

What Causes Seafloor Flattening?

Jay Haley¹

¹Department of Earth Science and Engineering, Imperial College London, South Kensington, London, United Kingdom

This manuscript was compiled on January 14, 2025. This report is submitted as part requirement for the MSci degree in Geology at Imperial College London. It is substantially the result of my own work except where indicated explicitly in the text. The report may be freely copied and distributed provided the source is acknowledged explicitly. This report was conducted under the supervision of Dr. Frederick Richards.

Word Count: 4489

Abstract

Bathymetric and heat flow measurements indicate that the oceanic lithosphere reaches a steady state thickness at ages that differ between the ocean basins. Even though this 'seafloor flattening' signal has been recognised in these datasets for over half a century, the physical mechanism responsible for causing this trend remains highly disputed. Here, I identify and quantify the primary processes responsible for seafloor flattening by evaluating each candidate mechanism in depth. The candidate mechanisms includes dynamic topography, mantle rejuvenation via plume interaction with the lithosphere and small-scale convection. First, I show that the proposed age-dependent trends in sub-lithospheric temperature and dynamic topography associated with secular cooling do not appear to exist, suggesting that deep mantle dynamics play little role in generating flattening. Next, using global plate models, I demonstrate that the magnitude and spatial extent of lithospheric rejuvenation, while locally important, is insufficient to account for observed bathymetric signals on a basinwide scale. Finally, a strong correlation between lithospheric thickness and crustal thickness in old oceanic lithosphere reveals that the presence of hotter sub-ridge potential temperatures during initial lithospheric formation may influence the onset of small-scale convection (SSC). Melt-depletion modulated small-scale convection therefore appears to be the dominant mechanism controlling seafloor flattening. This inference is confirmed by the strong agreement between numerical SSC modelling model predictions and observed changes in SSC onset age between basins. Findings indicate that SSC is widespread beneath old oceanic lithosphere, explaining the success of plate cooling models in depicting observed age-dependent bathymetric trends.

Keywords: Half space cooling, plate cooling model, small-scale convection, mantle rejuvenation, dynamic topography.

E-mail address: Jay Haley: jh2521@ic.ac.uk

Received: January 14th, 2025

1. Introduction

The first model introduced to explain the age dependence of heat flow and bathymetry of oceanic lithosphere was the half-space cooling (HSC) model (Parker and Oldenburg, 1973; D. Turcotte and Oxburgh, 1967). The HSC model describes the oceanic lithosphere as a semi-infinite medium (or "half-space") that cools through vertical heat conduction (Figure 1a). As cooling progresses, the thickness of the thermal boundary layer (TBL) increases in proportion to the square root of its age. However, due to the increase in quality and volume of global bathymetric, seismic, and gravitational data, it became obvious that simple HSC models were inadequate to describe seafloor older than ~70–80 Ma. Observations of ship-board oceanic bathymetry and heat flow measurements (e.g., Parsons and Sclater, 1977; Stein and Stein, 1992) and insights from studies of residual depth anomalies (e.g., Crosby and McKenzie, 2009; M. J. Hoggard et al., 2017; F. Richards et al., 2018) indicated that the lithosphere doesn't continue to cool and subside indefinitely as the HSC model suggests, but instead reaches a steady-state thickness, leading to a 'flattening' of seafloor depths (F. Richards et al., 2020). A new model was developed to explain this 'flattening' behaviour called the plate cooling model (PCM) (Parsons and Sclater, 1977). The PCM assumes the lithosphere reaches steady-state thickness by maintaining a constant temperature at a fixed depth (~100 km; Parsons

and Sclater, 1977; McKenzie et al., 2005). Although the reality of seafloor flattening was identified over half a century ago and is now widely accepted, the physical mechanism responsible for resupplying heat to the base of the TBL remains highly disputed.

Across the candidate mechanisms to explain this behaviour, sub-lithospheric small-scale convection (SSC) is most commonly proposed (Richter, 1973; Richter and Parsons, 1975; McKenzie and Weiss, 1975; Parsons and Sclater, 1977) and the supporting evidence is increasingly persuasive, e.g., recent seismic tomographic imaging of associated structures (Eilon et al., 2022). SSC is characterised by localised convective cells, predicted to be aligned with absolute plate motion, called 'Richter' rolls (Figure 1b; Richter, 1973; Buck and Parmentier, 1986; Huang et al., 2003; Conrad and Lithgow-Bertelloni, 2006). SSC is expected to develop when cool dense lithosphere thickens sufficiently to pass a critical threshold (Buck and Parmentier, 1986; Ballmer et al., 2007), beyond which Rayleigh-Taylor instabilities are triggered that lead to convective overturns (Parsons and McKenzie, 1978; D. L. Turcotte and Schubert, 2002; Zaranek and Parmentier, 2004). This convective destabilisation thins the lithosphere, increasing heat flow into its base (Davaille and Jaupart, 1994; Huang and Zhong, 2005). While SSC can increase heat flux, sceptics such as Sleep (2011) suggest that the heat provided by SSC alone is insufficient to halt the seafloor subsidence at older ages (i.e., >70 Ma).

Alternatives to SSC have been proposed such as lithospheric uplift and reheating by hotspots (e.g., Crough, 1978; Heestand and Crough, 1981; Davies, 2011), which has been more recently termed the "lithosphere rejuvenation model" (Utada, 2019). This model suggests that as the lithosphere passes over a plume, an increase in basal heat flux occurs, leading to lithospheric thinning or "rejuvenation", as well as dynamic topographic uplift (Figure 1c; Li et al., 2004; Thoraval et al., 2006). Another explanation is related to the decay of radiogenic isotopes and secular cooling (e.g., T. Korenaga et al., 2021). As secular cooling progresses, and radiogenic heat production decreases, the mantle's overall heat flux is expected to have decreased over time (Humlera et al., 1999). As a result, it has been suggested that the older lithosphere will have received systematically more mantle heat over its lifetime. This potentially increases its present-day temperature and reduces its subsidence relative to the present-day mid-ocean ridge system, which leads to flattening (J. Korenaga, 2008, 2015). Expanding on this idea, T. Korenaga and Korenaga (2016) and T. Korenaga et al. (2021) recently suggested that secular cooling and reduction in radiogenic heating may result in systematically higher temperatures in the convecting mantle beneath older oceanic lithosphere. This leads to an increase in dynamic topography at old ages that may explain observed flattening (Figure 1d).

While understanding the mechanisms of seafloor flattening is vital, attention must also be paid to the differences in their manifestation across oceanic basins. Significant differences are evident in the timing of seafloor flattening among the basins: flattening occurs around ~75 Ma in the Pacific, ~95 Ma in the Atlantic, and ~100 Ma in the Indian Ocean (F. Richards et al., 2020). These variations suggest that different mechanisms may be dominant in each basin (Lee et al., 2005; Crosby and McKenzie, 2009).

In recent discussions, researchers have emphasised the need to move away from simplistic cooling parametrisation in favour of models that directly incorporate physical mechanisms that could account for observed flattening, such as SSC, secular cooling and radiogenic heating (J. Korenaga, 2020). Determining which mechanisms contribute to seafloor flattening has far-reaching implications, not only for geodynamic

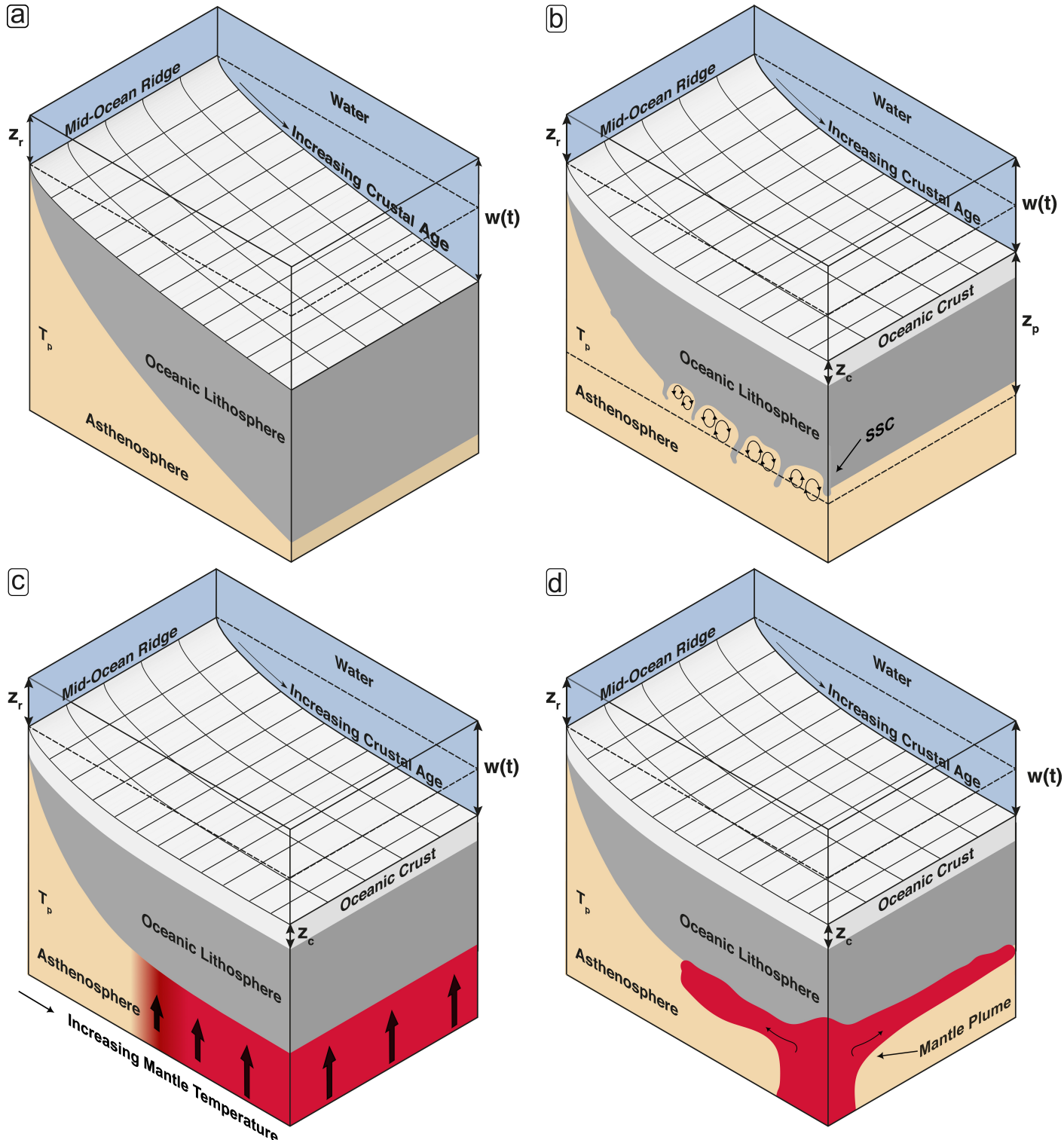


Figure 1. Thermal models of cooling oceanic lithosphere including potential mechanisms of flattening, modified after F. Richards et al., 2020. (a) The half-space cooling (HSC) model, where z_r is the zero-age ridge depth, T_p is the potential temperature of the asthenosphere, and $w(t)$ describes subsidence as a function of age. (b) The plate cooling model (PCM), where z_p denotes equilibrium plate thickness which is maintained by sub-lithospheric small scale convective destabilisation once the lithosphere thickens beyond a threshold value. (c) Deep ‘Dynamic topography’ model where flattening is caused by a systematic increase in depth-integrated sublithospheric mantle temperature with increasing crustal age. Increase in temperature illustrated with orange to red gradient. (d) ‘Lithospheric rejuvenation’ model where flattening occurs via mantle-plume-induced dynamic uplift and thermal erosion of the lithosphere.

modelling of subduction and dynamic topography but also for interpreting seismic tomography data, understanding melt generation processes beneath mid-ocean ridges and constraining Earth's long-term heat flow and energy budget. Furthermore, an improved framework for linking basin-specific subsidence trends to their underlying causes will inform reconstructions of paleoceanographic conditions and long-term sea-level changes.

I seek to quantitatively determine which mechanisms are primarily responsible for observed seafloor flattening by integrating comprehensive analysis of geophysical data from the Pacific, Atlantic, and Indian Oceans with empirical and numerical models. First, I determine whether deep mantle dynamics could be the primary driver of the observed bathymetric flattening with age (as proposed by T. Korenaga et al., 2021). Secondly, I quantify the extent to which lithosphere rejuvenation via plume activity can account for observed flattening. Next, I investigate the correlation between the onset age of seafloor flattening and mid-ocean ridge paleo-temperatures. Finally, I build 2D geodynamic models to test whether the observed relationships between basins can be linked to changes in SSC onset age caused by mantle temperature-induced variations in the depth extent of sub-ridge melt depletion and elevated compositional viscosity.

2. Dynamic Topography

2.1. Methods

T. Korenaga et al. (2021) proposed that secular cooling and reduced radiogenic heating may lead to systematically higher mantle temperatures throughout the convecting mantle beneath older oceanic lithosphere, leading to increasingly positive dynamic topography with age causing seafloor flattening. To test this proposed age-dependent trend in sub-lithospheric temperature and dynamic topography, the instantaneous flow kernel approach outlined in F. D. Richards et al. (2023) was used to predict present-day dynamic topography signal associated with buoyancy anomalies below the cooling TBL (>250 km depth). Mantle flow simulations employed 15 density models, each optimised to simultaneously fit present-day dynamic topography, geoid, and core-mantle boundary (CMB) excess ellipticity observations given a particular input seismic tomographic model and radial mantle viscosity profile (see 'Compositional inversions' in F. D. Richards et al. (2023) for details). Importantly, these observationally constrained models account for compositional heterogeneity associated with large low-velocity provinces (LLVPs) in the deep mantle, spurious long-wavelength structure in the mid-mantle from vertical smearing artefacts in tomographic inputs, and the non-linear temperature dependence of shear wave velocity due to anelastic effects. Present-day dynamic topography was then calculated for each model up to spherical harmonic degree, $l = 30$ ($\sim 1,000$ km wavelengths), excluding density anomalies above 250 km depth to avoid contamination of any systematic temperature signal associated with lithospheric cooling.

To explore potential age dependence in dynamic topography predictions, model outputs were globally binned by crustal age in 2 Ma increments (Figure 2c), using the polygon dataset of M. J. Hoggard et al. (2017) to exclude regions with bathymetric anomalies unrelated to plate cooling (e.g., fracture zones), ensuring better comparability with basement depth datasets that avoid such features. Binning was also performed for individual ocean basins for interoceanic comparisons (Figure 2e,g,i). To assess whether age-dependent dynamic topography signals could explain observed bathymetric flattening, they were

added to an optimal HSC model of F. Richards et al. (2020) and compared with measured basement depths (F. Richards et al., 2018). For each comparison, dynamic topography values were first binned by age into 2 Ma intervals across all 15 models, calculating the mean and standard deviation within each bin. The final average and standard deviation were then determined by aggregating the intermodel variations across these binned results, illustrating uncertainties associated with intermodel variability (Figure 2d,f,h,j).

2.2. Results

The relationship between dynamic topography (a proxy for depth-integrated sublithospheric mantle temperature variation) and age varies regionally. Globally, oceanic dynamic topography negatively correlates with age ($r = -0.47$, $R^2 = 0.22$; Figure 2c) with similar trends in the Pacific Ocean ($r = -0.46$, $R^2 = 0.21$; Figure 2e) and a weaker correlation in the Atlantic ($r = -0.26$, $R^2 = 0.07$; Figure 2g). Interestingly, the Indian Ocean deviates from this global pattern, showing a positive correlation ($r = 0.40$, $R^2 = 0.16$; Figure 2i). Notably, all observed correlations are weak and associated with small gradients (~ 0.002 km/Ma).

At the oldest basin ages, discrepancies between HSC model predictions and observed basement depths show that large positive dynamic topography is needed to explain deviations. These differences and their standard deviations are calculated by combining the uncertainties from the HSC model and observed residual depths (See Table 1).

Region	Age (Ma)	Difference (km)
Pacific Ocean	182	1.68 ± 0.19
Indian Ocean	158	1.33 ± 0.36
Atlantic Ocean	198	1.49 ± 0.42
Global	198	1.55 ± 0.46

Table 1. An interbasin comparison differences between HSC model predictions and observed basement depths for the oldest ages in each region. The Pacific Ocean exhibits the largest difference (Figure 2f), while the Indian Ocean shows the smallest difference with greater variability (Figure 2j). The Atlantic Ocean falls between the two, with a moderate difference and variability (Figure 2h). Globally, large positive dynamic topography is needed to explain these deviations from the HSC model at old seafloor ages (Figure 2d).

2.3. Discussion

Negative correlations between age and dynamic topography challenge the model of T. Korenaga et al. (2021), which requires a positive correlation, a trend not observed globally. Even in the Indian Ocean, where dynamic topography rises systematically at older ages (Figure 2j), the offset between the HSC and the observed basement depth beyond ~ 100 Ma is too large to be explained by dynamic topography alone (e.g., Flament et al., 2013).

Nevertheless, dynamic topography can cause substantial deviations from the basement depth evolution predicted by PCMs. In the past, shoaling of Pacific basement depth between 80–130 Ma has been attributed to the onset of SSC (Crosby et al., 2006; Crosby and McKenzie, 2009). However, Pacific dynamic topography significantly increases between 80–130 Ma, suggesting that the observed shoaling of basement depths results from convective processes below, rather than within, the cooling TBL (>250 km depth; Figure 3). Similarly, Crosby et al. (2006) inferred basement depth shoaling in the Northwest Atlantic at similar ages. However, predicted dynamic topography in this region opposes this interpretation, consistent

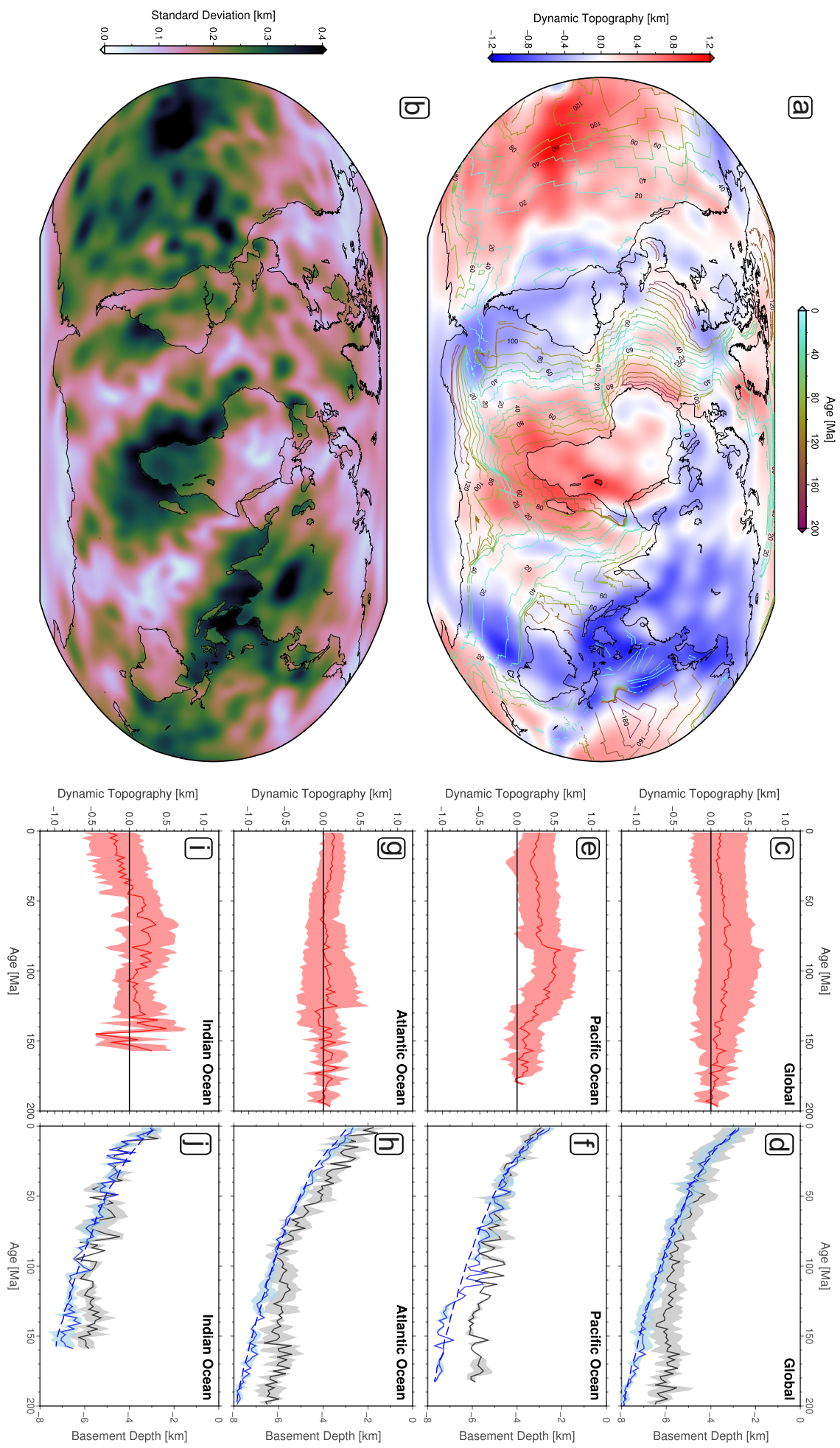


Figure 2. Inter-basin comparison of dynamic topography trends. (a) Geographic representation of predicted present-day dynamic topography for density anomaly contributions from the core-mantle boundary up to 250 km depth (i.e., below the cooling oceanic thermal boundary layer) averaged from the suite of optimised models from F. D. Richards et al. (2023). (b) Global map of uncertainties between 15 dynamic topography models shown as a standard deviation. (c) Red line/envelope = mean and standard deviation of present-day dynamic topography as a function of age, binned globally at 2 Ma intervals. Regions of anomalous crust are removed using polygons outlined in M. J. Hoggard et al. (2017). (d) Black line/grey envelope = global mean and standard deviation of water-loaded basement depths (F. Richards et al., 2018) binned globally at 2 Ma. Blue solid line/envelope = mean and standard deviations of dynamic topography at observed basement depth locations, added to the optimal HSC model of F. Richards et al. (2020); blue dashed line = half space cooling model (F. Richards et al., 2020). (e) Pacific dynamic topography subset. (f) Pacific subset of subsidence trends. (g) Atlantic dynamic topography subset. (h) Atlantic subset of subsidence trends. (i) Indian dynamic topography subset. (j) Indian subset of subsidence trends.

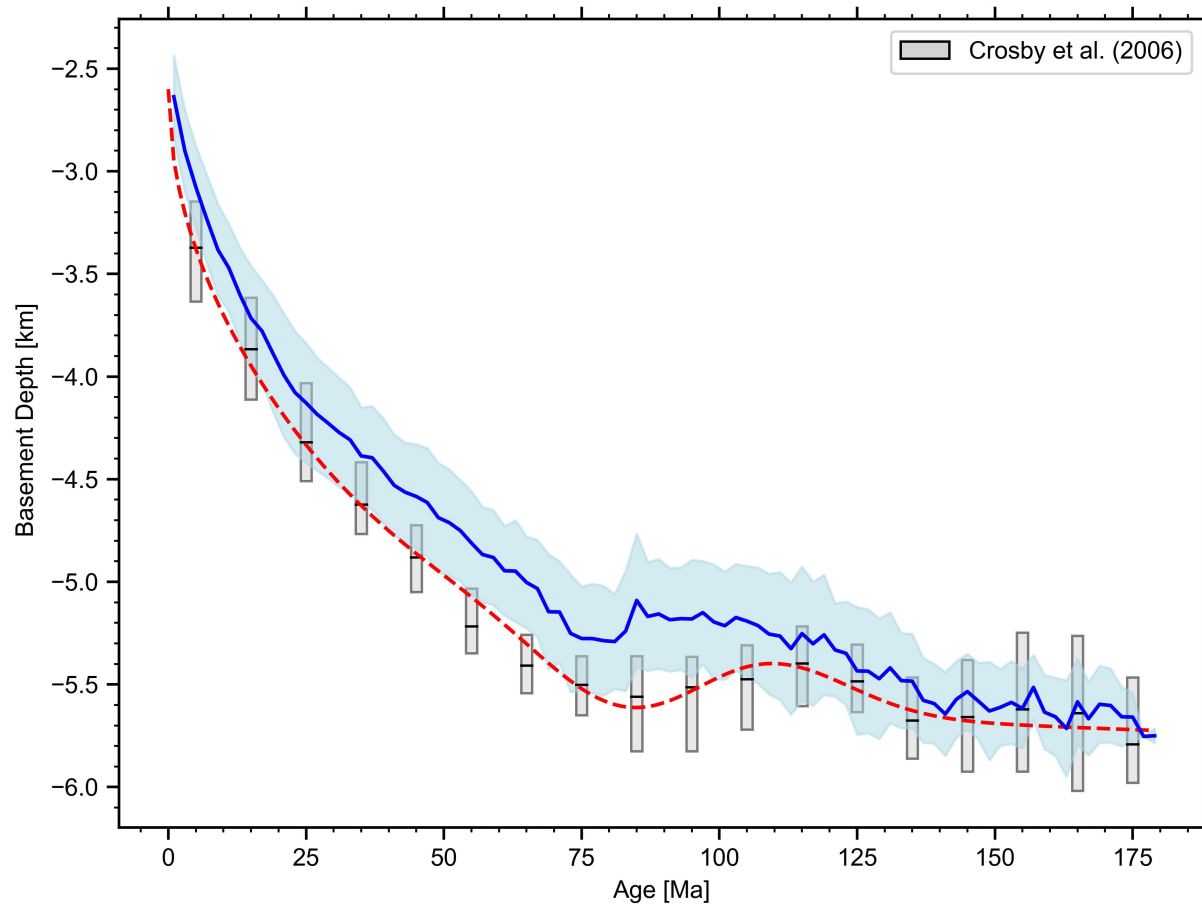


Figure 3. Observed shoaling between 80 - 140 Ma from the Crosby et al. (2006) dataset and predicted signal from present-day dynamic topography added to an optimised plate cooling model. Blue line/envelope = mean and standard deviation from optimised Pacific plate cooling model (Crosby et al., 2006) with added present-day dynamic topography signal as a function of age from the Pacific subset (see Figure 2e); grey boxes = upper bounds and lower bounds represent the interquartile range with a dashed black line representing the median of basement depths from Crosby et al. (2006); red dashed line = fitted line through basement depth data (Crosby et al., 2006).

with observations from Winterbourne et al. (2009). Finally, if the shoaling signal results from dynamic topography rather than SSC, as appears to be the case, it would be a region-specific phenomenon rather than a global one, as concluded here, and by Winterbourne et al. (2009).

Overall, this study finds no observational support for the predicted secular-cooling-induced increase in dynamic topography with lithospheric age that underpins the T. Korenaga et al. (2021) “reference model”. Another limitation of this model relates to their data filtering approach, which results in minimal sampling of lithosphere older than 100 Ma which limits their analysis to ages ≤ 150 Ma. Beyond 100 Ma, their data oscillates around the reference model, attributed to perturbations from SSC. However, a similar oscillatory signature appears in Indian Ocean dynamic topography predictions (Figure 2i,j), the source of most of their older data. Consequently, the signal in their “reference model” might reflect a local dynamic topography signal specific to the Indian Ocean, rather than a robust global trend.

3. Lithospheric Rejuvenation

3.1. Methods

3.1.1. Conceptual model

Having demonstrated that age-dependent trends in dynamic topography from deep mantle flow (i.e., below 250 km depth) weakly explain seafloor flattening, I explore the likelihood that lithospheric rejuvenation via mantle plumes is responsible. Clear evidence of lithospheric rejuvenation (i.e., shoaling of oceanic basement caused by asthenospheric upwelling and lithospheric thinning) can be observed in residual depth anomaly datasets (e.g., Holdt et al., 2022). These datasets show anomalously elevated bathymetry near hotspot loci, decreasing systematically with distance and time elapsed since the last hotspot interaction. Using this relationship, a 2D Gaussian function can be fitted to the residual depth anomaly data to describe the effect of mantle hotspots on basement depth on a global scale and in the three major basins

$$\Delta z = A \cdot \exp \left(- \left(\frac{D^2}{2\sigma_D^2} + \frac{T_{hs}^2}{2\sigma_{T_{hs}}^2} \right) \right), \quad (1)$$

where, Δz represents the plume-influenced residual depth anomaly as a function of distance from the hotspot, D (Figure 4a,c), and time elapsed since the last hotspot interaction, T_{hs} (Figure 4b,d). A is the maximum residual depth anomaly amplitude, while σ_D and $\sigma_{T_{hs}}$ represent the extent of hotspot-affected bathymetry in terms of D and T_{hs} , respectively. A 2D Gaussian function was chosen as a flexible representation of how hotspot influence diminishes both spatially and temporally from the hotspot loci.

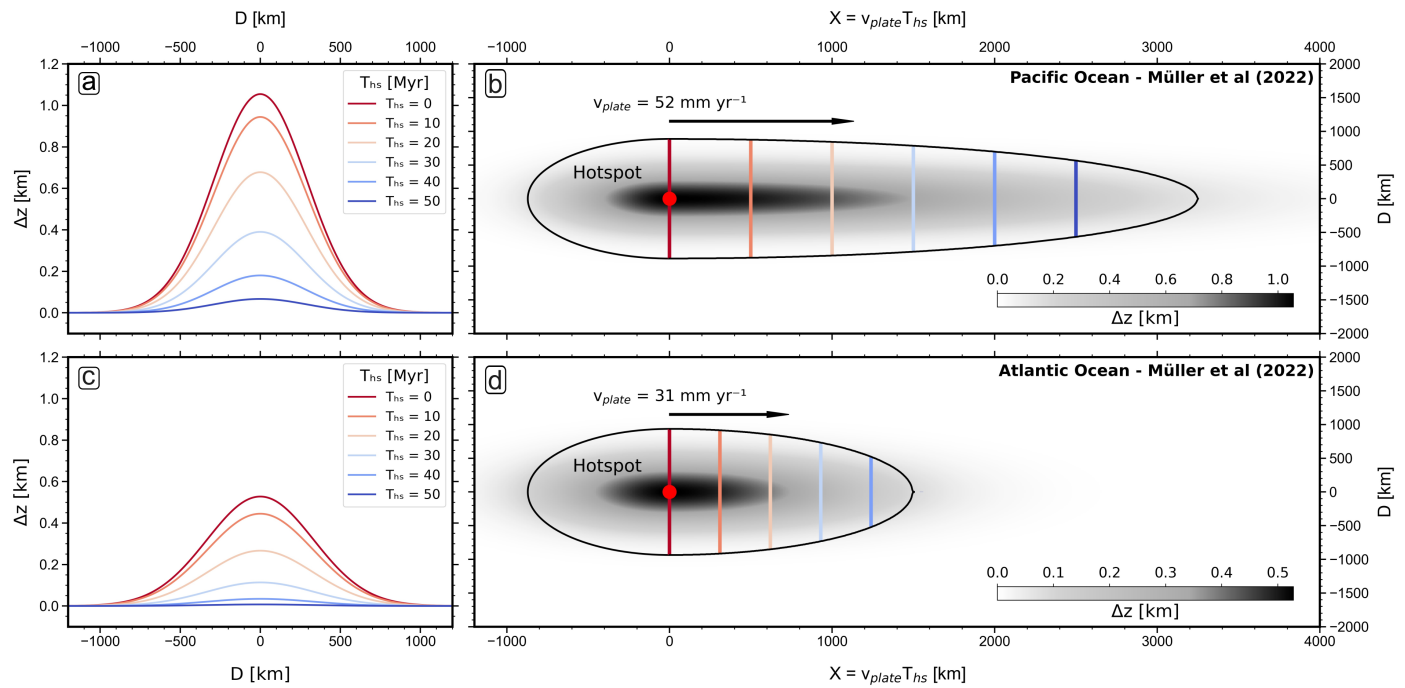


Figure 4. Visualisation of how predicted rejuvenation-induced residual depth anomalies (Δz), change as a function of distance from hotspot and time elapsed since last hotspot interaction. (a) Fitted curves using optimised parameters for the Pacific Ocean subset (using rotation files from Müller et al., 2022) showing how Δz decreases as a function of age. Solid coloured lines = time elapsed since the last hotspot interactions (T_{hs}) with warmer colours representing younger interaction times. (b) Black solid line = 10 m Δz contour; black to grey gradient = decay of Δz with increasing distance from hotspot track; red dot = present-day hotspot location; arrow = plate motion direction with accompanying basin average half-spreading rate calculated using ocean basin polygons (M. J. Hoggard et al., 2017) and grid of spreading rates (Seton et al., 2020). (c) Same as (a) but for the Atlantic Ocean. (d) Same as (b) but for Atlantic Ocean.

3.1.2. Plate Reconstructions

To apply the conceptual model, global absolute plate motion models and GPlates (version 2.5, Müller et al., 2018) were used to reconstruct hotspot tracks, calculated using two plate models with different mantle reference frames. The first model, introduced by Müller et al. (2022) (M22), employs a tectonic-rules-based ‘optimised’ mantle reference frame (Tetley et al., 2019), minimising net lithospheric rotation to $<0.25^\circ/\text{Myr}$ by integrating constraints from hotspot misfit analysis, trench dynamics, plate velocities, and net lithospheric rotation (Figure 5a). The second model, developed by Zahirovic et al. (2016) (Z16) as a revised version of Müller et al. (2016), utilises a hybrid reference frame. This hybrid reference frame adopts a fixed hotspot-based approach for times younger than $\sim 70 \text{ Ma}$ (Torsvik et al., 2008) and transitions to a true-polar-wander-corrected paleomagnetic reference frame developed by Steinberger and Torsvik (2008) for ages $>70 \text{ Ma}$. Which incorporates constraints from tomographically imaged slab remnants for improved accuracy (Figure 5b). Comparing these models tests the sensitivity of the results to different underlying plate reconstruction assumptions.

3.1.3. Hotspot Flowlines

I employed GPlates to extract equivalent total rotation (ETR) parameters from each plate motion model at 1 Myr intervals spanning 200 Ma to present, covering the age range of oceanic lithosphere (Müller et al., 2008). These ETR parameters reconstructed relative motion between the plates in each ocean basin and underlying mantle plumes back to the Jurassic period. Present-day hotspot locations (M. J. Hoggard et al., 2020) and ETR files were combined to determine hotspot flowlines for all oceanic plates using the backtracking technique described by Wessel (1999). Combined with a lithospheric age grid (F. Richards et al., 2018), these flowlines determined the time elapsed since the closest hotspot approach (T_{hs}) and associated distance to the hotspot (D) for all oceanic locations. Next, flowlines were isolated for individual tectonic plates using plate boundary data from Young et al. (2019), facilitated by the plate-specific total reconstructions. In instances where an oceanic location is intersected by multiple hotspot flowlines, the hotspot whose closest approach was most recent is selected. To ensure accuracy in resultant grids, only flowlines that approach within 500 km of the hotspot’s palaeolocation were considered. After all filtering steps, data grids of T_{hs} and D were obtained for all oceanic locations

3.1.4. Calculating Effects of Thermal Rejuvenation

After obtaining global predictions of T_{hs} and D , these datasets were sampled at the locations of residual depth anomaly data (Δz ; Holdt et al., 2022) and fit to the parameterisation in Equation 1. To reduce uncertainties associated with their choice of reference plate cooling model, I excluded residual depth data from seafloor younger than 70 Ma. An additional filter retained only data points potentially influenced by recent plume interaction. Specifically, all locations with $T_{hs} \leq 10 \text{ Ma}$ or $D \leq 100 \text{ km}$ and $10 \text{ Ma} \leq T_{hs} \leq 100 \text{ Ma}$. These thresholds were chosen since they minimised the average misfit between the optimal parameterisation and the filtered input data.

Optimal values for A , σ_D , and $\sigma_{T_{hs}}$ were obtained using the Levenberg-Marquardt algorithm in `scipy`, with initial guesses of 1.0, 200.0, and 40.0, respectively. The coefficient of determination (R^2) was used to evaluate how well the model fitted by quantifying the amount of variance explained by the independent variables. The resulting best-fit parameters and respective uncertainties provide a quantitative framework

for estimating plume-induced thermal rejuvenation on basement depths throughout the global ocean.

Combining D and T_{hs} grids, with the fitted parameters A , σ_D , and $\sigma_{T_{hs}}$, I generated predicted rejuvenation-induced basement depth deflections (Δz) for each ocean basin based on the parameterisation in Equation 1. These deflections were added to a global prediction of HSC-induced basement depth evolution (F. Richards et al., 2020) to investigate whether the combined model predictions could reproduce the observed flattening of basement depths (F. Richards et al., 2018). A sensitivity analysis was also performed by recalculating the predicted basement deflections after adjusting each fitted parameter by $\pm 1\sigma$, to assess how each parameter uncertainties affect the final model's ability to describe seafloor flattening (Figure 5).

3.2. Results

Both plate reconstructions produced consistent best-fit parameters and rejuvenation signatures across all basins. However, the M22 model consistently outperformed that of Z16 (See Appendix 1), achieving higher R^2 values (e.g., 0.57 vs 0.41 in the Pacific Basin). Therefore, this study focuses exclusively on rejuvenation predictions on the M22 plate reconstructions (Figure 5a). Fitting the 2D Gaussian model to the residual basement depths produces a clear spatiotemporal signature of rejuvenation near oceanic hotspots. Across oceanic basins, residual basement depths systematically decreased with distance from the hotspot loci and increased time elapsed since the last hotspot interaction (Figure 6; See Table 2).

Parameter	Global	Pacific	Atlantic	Indian
Amplitude (A) [km]	0.64 ± 0.04	1.05 ± 0.06	0.53 ± 0.06	0.48 ± 0.09
Critical Distance (σ_D^2) [km]	332 ± 24	290 ± 16	332 ± 24	675 ± 216
Critical Time Hotspot Interaction ($\sigma_{T_{hs}}^2$) [Ma]	20 ± 2	21 ± 2	17 ± 4	34 ± 16
R^2	0.28	0.57	0.21	0.23

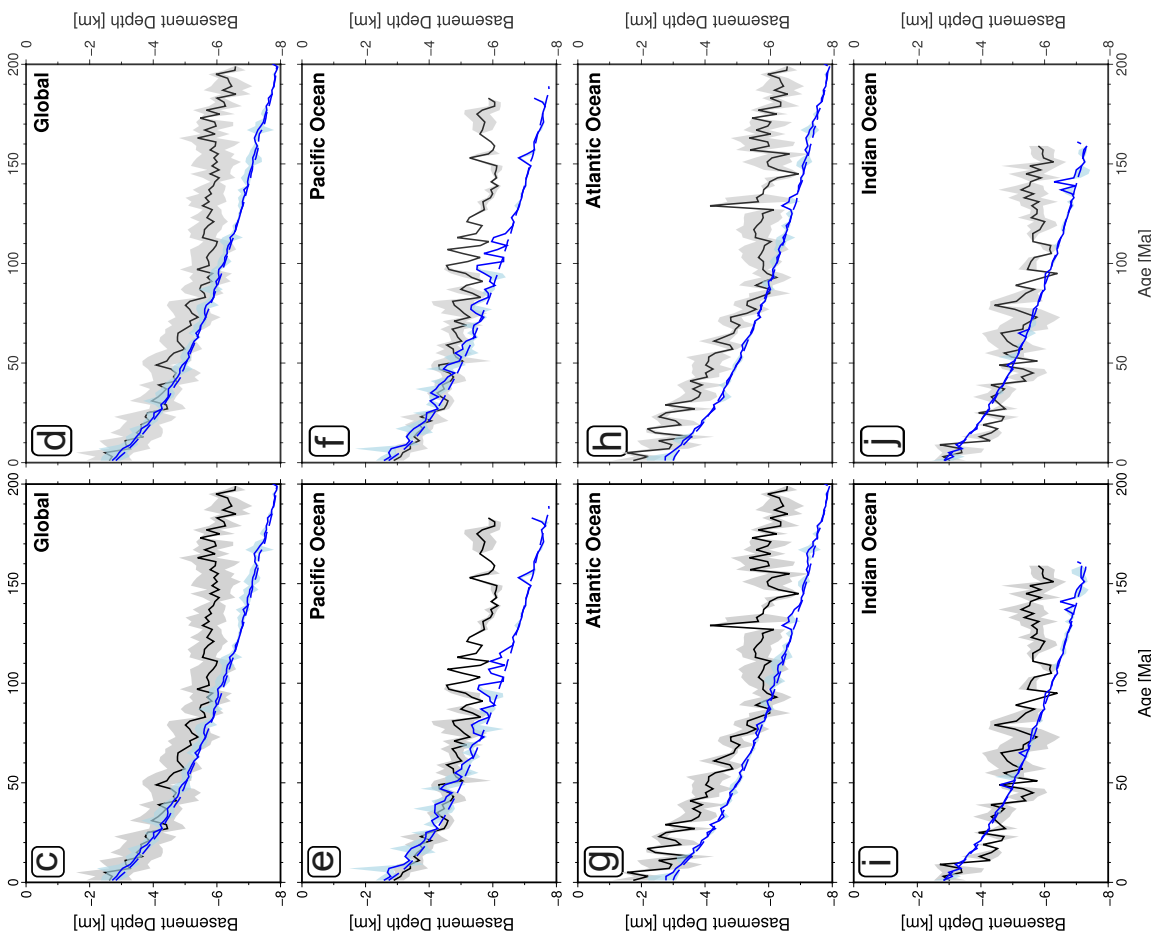
Table 2. Summary of parameter fitting results for residual basement depth data (Holdt et al., 2022) globally and across the Pacific, Atlantic, and Indian basins. The Pacific basin (Figure 6c,d) showed the highest best-fit amplitude (A), while the Atlantic and Indian basins showed systematically lower values (Figure 6e,f,g,h). The critical distance (σ_D^2), was smallest in the Pacific (Figure 6c), intermediate in the Atlantic (Figure 6e), and largest in the Indian basin (Figure 6g). Similarly, the critical time elapsed since last hotspot interaction varied ($\sigma_{T_{hs}}^2$), with the Indian basin (Figure 6h) displaying the longest duration, while the Pacific and Atlantic basins had shorter timescales (Figure 6d,f). Correlation strength, indicated by R^2 values, were highest in the Pacific, with notably weaker correlations in the Atlantic and Indian basins.

The age of the largest deviations from the HSC cooling trend due to lithospheric rejuvenation are observed in the Pacific at 97 Ma and 99 Ma (both 0.66 km; Figure 5e); in the Atlantic at 129 Ma (0.28 km) and 3 Ma (0.27 km; Figure 5g); and in the Indian basin at 141 Ma (0.53 km) and 49 Ma (0.40 km; Figure 5i).

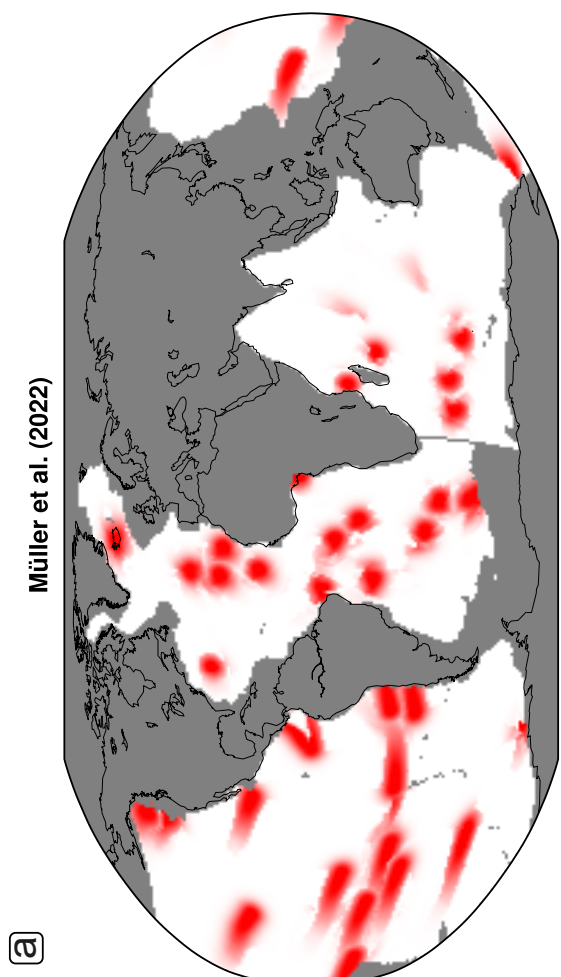
3.3. Discussion

Before analysis, it was expected that residual depth anomalies around Atlantic basin hotspots would be systematically higher than those in the Pacific. This is thought to be attributed to lower plate velocities in this basin, which prolong plume-lithosphere interaction times and the extent of lithospheric thinning (Monnereau et al., 1993). However, modelling results indicate a lower best-fitting amplitude (A) in the Atlantic. Two factors may help explain this contradiction. First, Atlantic plumes on lithosphere older than 70 Ma (the age cut-off used in the fitting process outlined above) have a buoyancy flux approximately 78% lower than

Zahirovic et al. (2016)



Müller et al. (2022)



Zahirovic et al. (2016)

Figure 5. Inter-basin comparison between modelled rejuvenation trends. (a) Map of predicted rejuvenation-induced basement depth deflections (Δz) for Müller et al. (2022) global plate reconstruction. Grey areas = excluded areas using polygons from M. J. Hoggard et al. (2017); white areas = regions unaffected by mantle rejuvenation. (b) Same as (a) for Zahirovic et al. (2016) global plate model. (c) Observed and predicted basement depth evolution using Müller et al. (2022) plate reconstruction. Black line/grey envelope = global mean and standard deviation of water-loaded basement depths (F. Richards et al., 2018) binned at 2-Ma intervals; blue solid line/envelope = mean and standard deviations of rejuvenation-induced basement depth deflection at observed locations, added to the optimal HSC model of F. Richards et al. (2020); blue dashed line = optimal half space cooling model (F. Richards et al., 2020). (d) Same as (c) for Zahirovic et al., 2016 global plate model. (e, g, & i) Same as (c) for Pacific, Atlantic, and Indian Ocean, respectively. (f, h, & j) Same as (d) for Pacific, Atlantic, and Indian Ocean, respectively.

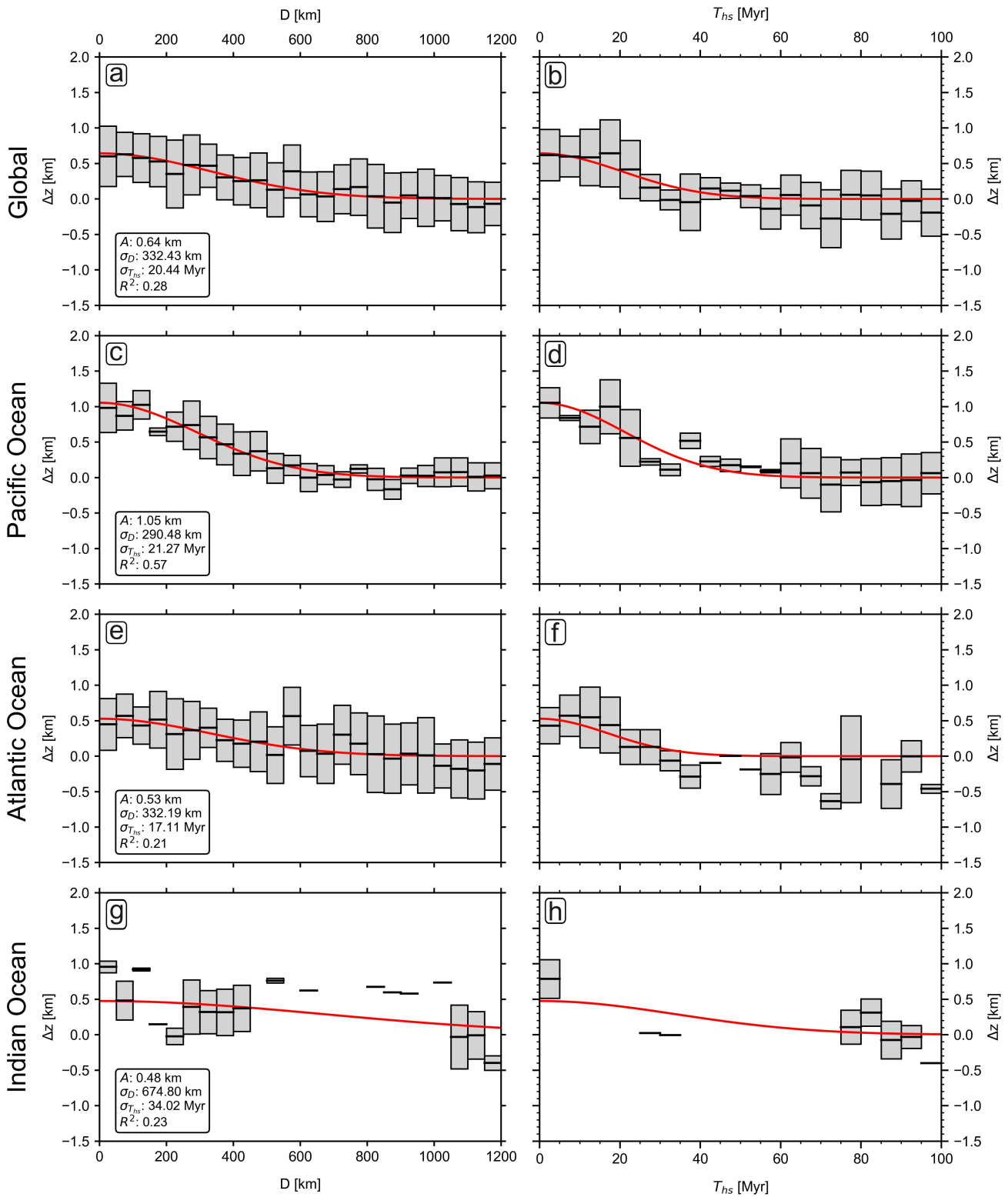


Figure 6. Optimised fits to global and basin-specific residual depth anomaly datasets (Holdt et al., 2022) using the global plate model Müller et al. (2022). (a) Global dataset. Red line = fit of 2D to residual depth anomalies as a function of distance away from hotspot track (D); grey box = standard deviation with black horizontal line representing the mean, binned at 50-km intervals. The fitted parameters—amplitude in km (A), critical distance in km (σ_D), critical time ($\sigma_{T_{hs}}^2$) and the coefficient of determination (R^2)—are annotated in the bottom left. (b) Same for time elapsed since last hotspot interaction (T_{hs}), binned at 5-Myr intervals. (c, e, & g) Same as (a) for Pacific, Atlantic, and Indian datasets, respectively. (d, f, & h) Same as (b) for Pacific, Atlantic, and Indian datasets, respectively.

Pacific plumes of similar age (Agrusta et al., 2013, 2015). Reduced upwelling velocities and temperature excesses limit dynamic support and lithospheric thinning efficiency, ultimately outweighing the topographic impact of longer plume-lithosphere interaction times. Second, the fitted Atlantic parameterisation likely underestimates the rejuvenation signal because residual depth anomalies tend to decay below zero at large distances (D) and long times since the last plume interaction (T_{hs} ; Figure 6e,f). This negative offset prevents the parameterisation—which assumes residual depth change tends to zero at high D and T_{hs} values—from capturing the full amplitude of the residual depth signal associated with Atlantic plumes. Since the offset does not appear related to deep mantle dynamic topography (See Figure 2g), it likely reflects delayed SSC onset in the Atlantic, causing additional subsidence compared to the global reference PCM used to define the residual depth anomalies. This results in systematically more negative residual depth anomalies in old age. Regardless of its cause, when this trend is compensated for by adopting values of upper-bound parameters in the Atlantic, the resulting mantle rejuvenation signal remains insufficient to explain the observed flattening.

Observations of residual depth decay over time align with other studies. By examining swell bathymetry and island submergence at 14 major ocean hotspots, Huppert et al. (2020) found that plume-associated excess topography has largely disappeared within ~ 35 Myr of the last hotspot interaction. Using a different approach, M. J. Hoggard et al. (2017) recorded a characteristic swell decay time of ~ 40 Ma around hotspots. Both observations are consistent with the $\sigma_{T_{hs}}$ values in this study.

Utada (2019) used numerical modelling to argue that seafloor depth data alone cannot distinguish between flattening caused by SSC or lithospheric rejuvenation. Their results suggest that if lithosphere rejuvenation occurs early and endures long enough, it can mimic the seafloor topography predicted by PCMs (which approximate SSC effects). However, their theoretical approach has two key limitations. Firstly, they infer the time interval over which thermal rejuvenation interrupts lithospheric cooling to be ~ 60 Myrs, >20 Myr longer than the $\sim 20\text{--}40$ Ma swell decay times obtained here and in other studies. Secondly, they assume the plume-lithosphere interaction ends before 70 Ma. In their model, any plume affecting the lithosphere at greater ages would not be able to match the shallow seafloor depths predicted by the PCM because their assumed rejuvenation signal simply stalls HSC-like subsidence at a fixed basement depth and, beyond 70 Ma, the HSC model predicts deeper basement depths than the PCM.

Overall, while thermal rejuvenation may help explain seafloor flattening up to 100 Ma in the Pacific, its contribution to broader global patterns is minimal, particularly in the Indian and Atlantic basins where lower plate velocities restrict the extent of thermal rejuvenation.

One limitation of this approach is the assumption that all mantle hotspots exert equivalent rejuvenation effects on the lithosphere when, in reality, plume buoyancy flux can vary substantially spatially and temporally. For instance, Vidal and Bonneville (2004) estimated that the Hawaiian hotspot buoyancy flux has increased roughly fivefold in the past 30 Ma. Despite this variability, unless buoyancy flux has changed systematically through time on global or basin-wide scales, this approach should produce robust estimates of average age-dependent trends in lithospheric rejuvenation, while reducing sensitivity to the often poorly constrained buoyancy flux variations of individual hotspots.

4. Small Scale Convection

4.1. Methods

4.1.1. Crustal Thickness-Lithospheric Thickness Relationship

Ma and Dalton (2019) propose that mantle potential temperature at mid-ocean ridges during lithosphere formation controls the subsequent timing of SSC onset, as it cools with age. This hypothesis is based on the observation that the initial depth of melting beneath the ridge increases with mantle potential temperature. The thickness of the dry, high-viscosity harzburgite layer that is left behind by the melting process and is subsequently frozen into the cooling oceanic lithosphere will, therefore, be systematically thicker when the sub-ridge potential temperature is hotter, acting to postpone SSC onset (Lee et al., 2005; Afonso et al., 2008). To test Ma and Dalton (2019)'s hypothesis, I compared co-located crustal thickness estimates (T_c) from seismic refraction studies (Christeson et al., 2019; F. D. Richards et al., 2020) with lithospheric thickness (T_l) from calibrated conversions of global seismic tomographic models (SL2013sv, Schaeffer and Lebedev, 2013; 3D2015-07Sv, Debayle et al., 2016; CAM2016, Ho et al. (2016); and SLNAAFSA, K. Hoggard et al., 2020) throughout the global ocean. To reduce short-wavelength T_c changes related to small-scale tectono-magmatic complexity rather than spatiotemporal mantle potential temperature variation, the data was binned into 1km intervals, consistent with typical measurement uncertainties (e.g., Herath et al., 2020). This binning defines underlying T_c - T_l relationships and stabilises correlations. Lithospheric thicknesses from the SL2013sv model yielded the strongest global correlations with T_c and was therefore selected for detailed basin-scale analyses. Utilising the methodology from Section 2.1, I used M. J. Hoggard et al. (2017) polygons to delineate ocean basins, and determined correlation coefficients for each.

4.1.2. 2D Modelling

Given the T_c - T_l trends appear to support the Ma and Dalton (2019) hypothesis, I explored the effect of depleted layer thickness on SSC onset time. Specifically, I examined whether depleted layer thicknesses and plate velocities required to explain varying SSC onsets between basins align with observed plate velocities and crustal-thickness-derived estimates of mantle potential temperatures and depleted layer thicknesses. Hence, I incorporated plate velocity variation representative of average basin velocities (Seton et al., 2020). Also, aligned with Ma and Dalton (2019)'s hypothesis, I systematically assessed the interplay between the effects of thickness and differential viscosity of a depleted layer.

Computations were done using ASPECT (code version 2.5.0, Bangerth et al., 2023; Heister et al., 2017; Kronbichler et al., 2012). I conducted 80 simulations within a 2D model domain with a 400 km vertical extent, scaling the horizontal extent according to the prescribed v_{half} to ensure ages at the right and left boundary reach an age of 200 Ma, aligned with the age of oldest oceanic lithosphere. Variable model parameters include the half-spreading rate v_{half} , compositional viscosity prefactor C_η , thermal viscosity exponent α_η , and depleted layer thickness (L_D ; See Table.3). The model assumed Newtonian rheology, where viscosity has temperature and depth dependence but not stress dependence.

The finite element mesh used to solve the underlying equations comprises three layers with decreasing resolution with depth. Vertical resolution is 3.125 km in the shallowest 7 km, 6.25 km in the intermediate layer between 7 km and the base of the depleted layer, and 12.5 km in the underlying deep layer. Horizontal resolution varies according to spreading velocity, v_{half} (in cm yr^{-1}) and is equal to $1.5625 \text{ km} \times v_{\text{half}}$,

Symbol	Meaning	Value(s)	Unit
t_{sim}	Simulation run time	500	Ma
L_x	Horizontal extent (box width)	$L_x = v_{\text{half}} \times 400 \text{ Ma}$	km
L_z	Vertical extent (box height)	400	km
T_{top}	Surface (top) temperature	293	K
T_{bot}	Bottom inflow temperature	1600	K
T_{ref}	Reference temperature for viscosity	1473	K
k	Thermal conductivity	4.7	$\text{W m}^{-1} \text{K}^{-1}$
c_p	Heat capacity	1250	$\text{J kg}^{-1} \text{K}^{-1}$
ρ_m	Reference density	3300	kg m^{-3}
α	Thermal expansivity	2×10^5	K^{-1}
$\Delta\rho_C$	Compositional density contrast	-30 [a]	kg m^{-3}
g	Gravitational acceleration	10	m s^{-2}
η_{ref}	Reference viscosity	1×10^{20}	Pa s
α_η	Thermal viscosity exponent	10, 20	—
C_η	Compositional viscosity prefactor	10, 100	—
L_D	Depleted layer thickness	30, 60, 90, 120, 150	km
v_{half}	(Half-)spreading rate	1, 4, 7, 10	cm yr^{-1}

Table 3. Key parameters for the 2D mid-ocean ridge spreading model. The domain is L_x km wide by 400 km deep, with a prescribed bottom temperature of 1600 K and a surface temperature of 293 K. The horizontal extent of the model was scaled so that the horizontal distance from the ridge to the model boundary equates to an age difference of 200 Ma (i.e., if $v_{\text{half}} = 10 \text{ cm yr}^{-1}$, the horizontal extent would be 40,000 km). Model runtime was set at 500 Myr to ensure the simulations reached a steady-state. Variable model parameters include the half-spreading rate v_{half} ; compositional viscosity prefactor C_η (range based on Ma and Dalton, 2019); thermal viscosity exponent α_η (range equivalent to 150–300 kJ mol $^{-1}$ activation energy, based on J. Korenaga, 2003 and Coltice and Shephard, 2018), and depleted layer thickness (L_D). [a]Shorttle et al. (2014). Cases with no depleted layer were also run. For a visualisation of these model parameters refer to Figure 7.

3.125 km \times v_{half} , and 6.25 km \times v_{half} in the shallow, intermediate, and deep mesh layers, respectively. This mesh structure is adopted to achieve the resolution necessary to accurately capture high velocity and temperature gradients near the ridge axis, while simultaneously minimising model runtime.

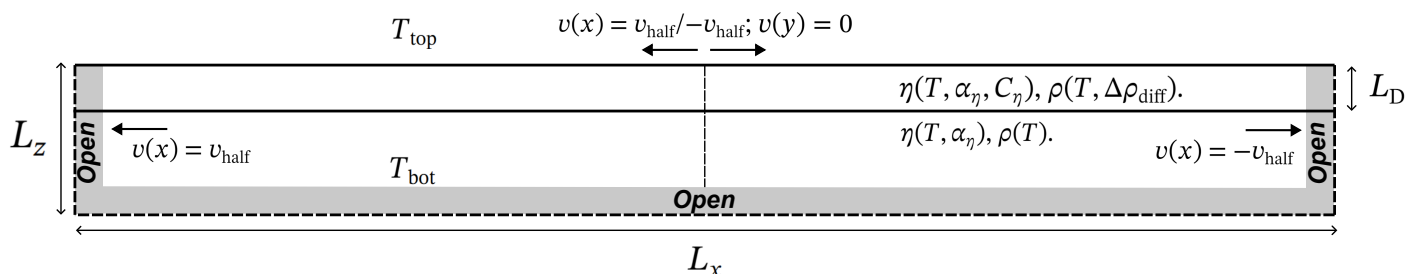


Figure 7. Boundary conditions for the small scale convection models, incorporating a spreading ridge system with a domain of L_x by L_z . The top layer represents a chemically depleted layer with a thickness of L_D . Grey/dashed line = Open boundary conditions. The top boundary is closed, hence the vertical velocity component = 0.

4.1.3. Predicted Onset Times and Depleted Layer Thickness

To investigate the onset time of small-scale convection (SSC) across the 80 unique models, I quantified the degree to which each model's numerically predicted lithospheric thermal evolution diverges from standard half-space cooling (HSC) predictions. Specifically, I used the 1200 °C isotherm as a proxy for lithospheric thickness (e.g., F. Richards et al., 2018) for all timesteps after 300 Myrs (i.e., after the model at steady state).

At each model timestep, the depth of the numerically predicted 1200 °C isotherm was compared with the corresponding depth predicted by the HSC equation (Equation 2). To account for horizontal heat conduction and temporal fluctuations in SSC-predicted isotherms, the thermal diffusivity, κ , used in the HSC predictions was optimised at each model timestep by minimising the misfit between HSC- and SSC-predicted isotherms. The HSC-predicted isotherms were calculated using

$$d(T) = \operatorname{erf}^{-1} \left(2\sqrt{\kappa t} \left[\frac{T_{\text{LAB}} - T_s}{T_m - T_s} \right] \right), \quad (2)$$

where, $\kappa = \frac{k}{\rho c_p}$, k is thermal conductivity, ρ is mantle density (3300 kg/m³), c_p is heat capacity, $T_{\text{LAB}} = 1200$ °C is the temperature of the lithosphere-asthenosphere boundary isotherm, T_s is the surface temperature (293 K), and T_m is the convecting mantle temperature (1600 K).

SSC onset time was then determined at each model timestep as the earliest time (beyond a model age of 30 Ma) when the depth difference exceeds 1 km between the 1200 °C isotherms predicted by the SSC model and the HSC prediction (now using a κ value obtained by averaging the optimised values).

To identify steady-state conditions, a running mean of the onset time was calculated, with the steady-state defined when the running mean varied by less than 0.01 Myr between consecutive timesteps. Median onset times and depths, along with their 16th and 84th percentile uncertainties, were calculated only from steady-state timesteps.

Observed crustal thicknesses from F. D. Richards et al. (2020) on lithosphere older than 70 Ma were subsequently used to predict depleted layer thickness in each basin. This prediction used the dry peridotite melting parameterisation of Shorttle et al. (2014) to calculate the relationship between oceanic crustal thickness and initial melting depth (z_{melt})—assumed to equate to the base of the depleted layer—for mantle potential temperatures between 1300 °C and 1600 °C. Basin-averaged crustal thicknesses could then be directly compared to those predicted by the melting calculation and used to infer corresponding depleted layer thicknesses ($L_D = z_{\text{melt}} - T_c$).

Absolute SSC onset times for each basin were calculated using observed basement depths (F. Richards et al., 2018) by quantifying the deviations from best-fitting HSC models. Divergence points were identified by incorporating basement depth uncertainties (See Appendix 2 for details).

4.2. Results

Results from T_C - T_l analysis indicate a strong global correlation ($r_b = 0.80$; Figure 8b), consistent with the Pacific ($r_b = 1.00$; Figure 8d) and Indian basins ($r_b = 0.90$; Figure 8h). However, the Atlantic basin shows a weaker correlation ($r_b = 0.30$), with high variability in lithospheric thicknesses across crustal thickness bins (Figure 8f).

Overall, C_η showed the weakest influence on SSC onset times, indicating that having any viscosity contrast is more crucial than its magnitude (Figure 9). Decreasing v_{half} from 10 to 1 cm yr⁻¹ generally delayed SSC onset, though for L_D values exceeding 30 km, the slowest v_{half} exhibited an inconsistent trend, showing the earliest SSC onset with high uncertainty (Figure 9). Despite this inconsistency, a strong relationship emerged between L_D and SSC onset times across all models, with SSC consistently occurring later as L_D increased (Figure 9). This trend is especially evident in models with $C_\eta=10$, $\alpha_\eta=10$, $v_{\text{half}}=7$ cm yr⁻¹, where increasing the L_D in 30 km intervals shifts onset time by approximately ~20 Ma (Figure 9a).

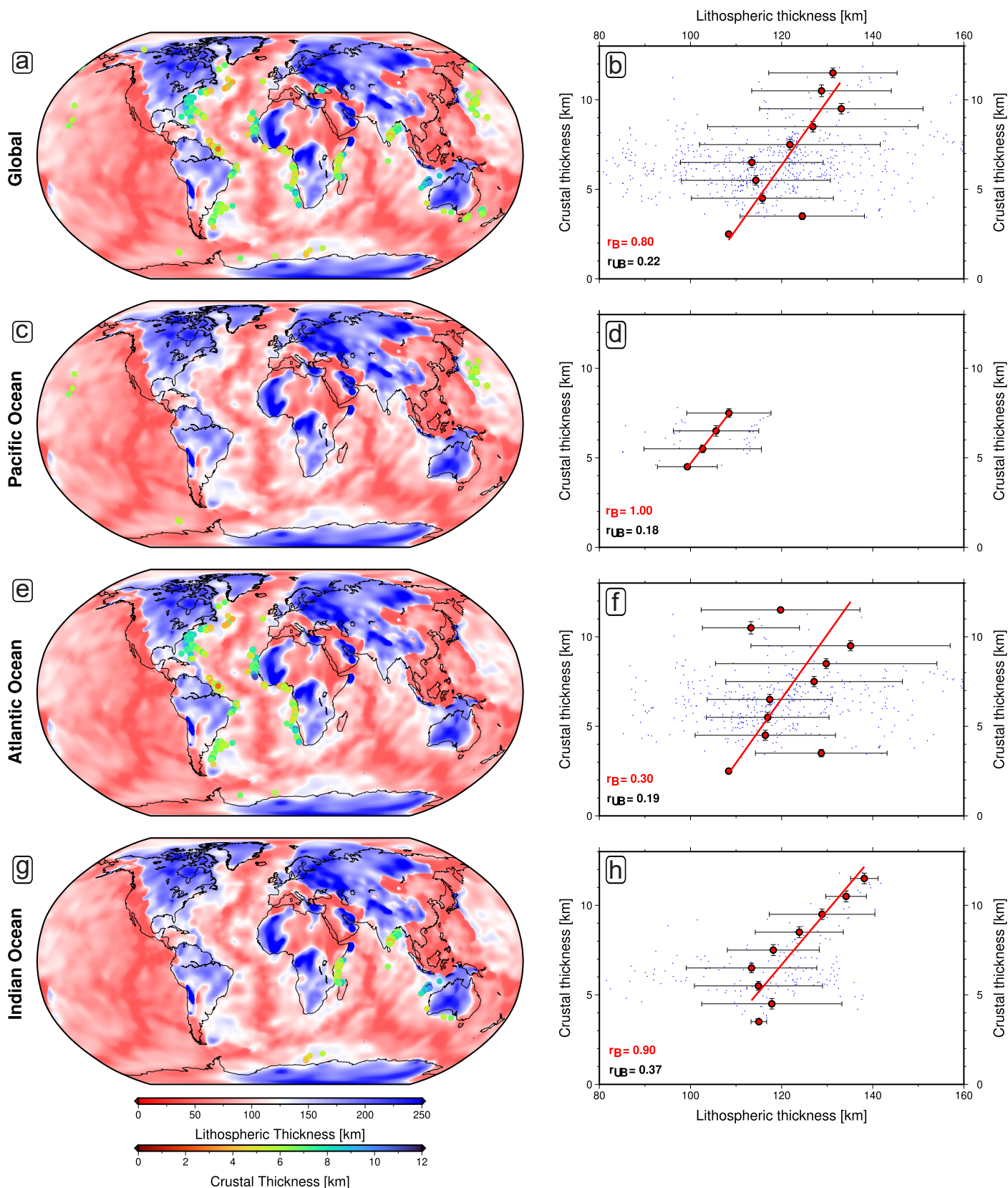


Figure 8. Inter-basin comparisons of crustal thickness versus lithospheric thickness. (a) Map of predicted present-day lithospheric thickness from SL2013sv seismic tomographic model (Schaeffer and Lebedev, 2013). Circles = locations of crustal thicknesses observations (Christeson et al., 2019; F. D. Richards et al., 2020) on lithosphere older than 70 Ma. Regions of anomalous crust are removed using polygons outlined in M. J. Hoggard et al. (2017). (b) Global relationship between oceanic lithospheric and crustal thicknesses. Blue circles = crustal and lithospheric thickness at all locations. Red circles/black lines = mean and standard deviation of 1-km crustal thickness bins; red line = line of best fit through binned data. The strength between the variables is quantified using Pearson's correlation coefficient, denoted as r_B for binned data and r_{UB} for unbinned data. (c, e, & g) Same as (a) for Pacific, Atlantic, and Indian Ocean, respectively. (d, f, & h) Same as (b) Pacific, Atlantic, and Indian Ocean, respectively.

Furthermore, α_η had the greatest effect on onset times for $L_D = 0\text{--}60$ km, delaying onset times by around ~ 15 Ma when increased from 10 to 20 (Figure 9c,d).

Maximum predicted palaeo-ridge axis potential temperatures (T_p) and depleted layer thickness (L_D) calculated from inter-basin crustal-thickness-variations showed a systematic increase in the Atlantic ($T_p = 1507$ °C, $L_D = 111$ km) and Indian Oceans ($T_p = 1499$ °C, $L_D = 108$ km) relative to the Pacific ($T_p = 1388$ °C, $L_D = 77$ km; Figure 9). This trend is also reflected in the 84th percentile with Atlantic ($T_p = 1379$ °C, $L_D = 74$ km) and Indian ($T_p = 1388$ °C, $L_D = 77$ km) compared to Pacific ($T_p = 1367$ °C, $L_D = 70$ km; Figure 9). Median ($T_p \sim 1353$ °C, $L_D \sim 67$ km), 16th percentile ($T_p \sim 1335$ °C, $L_D \sim 63$ km) and minimum potential temperatures ($T_p \sim 1300$ °C, $L_D \sim 54$ km) remained largely consistent between the three basins (Figure 9).

4.3. Discussion

Preliminary analysis strongly supports the hypothesis of Ma and Dalton (2019), showing that potential temperature anomalies at the ridge axis influence subsequent SSC onset and that these anomalies may have lasted over long timescales. However, the trend is less pronounced in the Atlantic basin, where a low T_c - T_l correlation indicates a weaker dependence of lithospheric thickness on mantle potential temperature at the time of formation (Figure 8). I propose that this discrepancy may result from lithospheric rejuvenation (Ribe, 2004), on thick, old (>70 Ma) lithosphere. Numerical modelling shows that the uplift of the lithosphere-asthenosphere boundary is a function of ascent rates within the plume conduit and the spatial extent of sublithospheric radial flow away from the plume, which are enhanced by slow plate speeds (e.g., Atlantic Basin) and high buoyancy fluxes (W m s^{-1} ; Agrusta et al., 2013). In Figure 10, I demonstrate that buoyancy fluxes in the Atlantic basin are relatively high when compared to the Indian basin over old lithosphere. Consequently, the combination of relatively high buoyancy fluxes and quantity of hotspots (compared to the Indian basin) likely enhances lithospheric rejuvenation and contributes to the stronger T_l variability in the Atlantic. This hypothesis is consistent with independent observations of rejuvenation on old (115–140 Ma) oceanic lithosphere at Cape Verde, where shear-wave velocity measurements imply that the present-day geotherm resembles that of ~ 30 Ma old lithosphere (de Carvalho, 2020). Lithospheric thinning is further supported by geochemical data, finding a T_l of ~ 60 km at Cape Verde and Canary hotspots, considerably thinner than the ~ 100 km expected for lithosphere of similar age (Ball et al., 2021). Similar trends may also affect Pacific T_c - T_l relationships, however, the available crustal-thickness observations are limited and mainly located away from plume-affected regions.

Having established that T_c -inferred palaeo-temperature anomalies at ridge axes correlate with the eventual thickness of the lithosphere they generate, I provide strong evidence that this relationship can be explained by the impact these thermal perturbations have on the extent of melt depletion beneath the ridge (L_D). Increasing L_D effectively delays SSC onset times, potentially explaining differences in SSC onset across the three ocean basins studied. I also show that higher plate velocities generally don't significantly influence SSC onset but SSC onset is lower at 1 cm yr^{-1} (Figure 11b,d,f,h), which is consistent with findings from 2D Newtonian simulations (van Hunen et al., 2003; Huang et al., 2003). Until recently (Eilon et al., 2022), there has been a lack of unambiguous detections of SSC-related structures. This study helps to explain this absence since, when plate velocity exceeds $\sim 1 \text{ cm yr}^{-1}$, the average predicted width

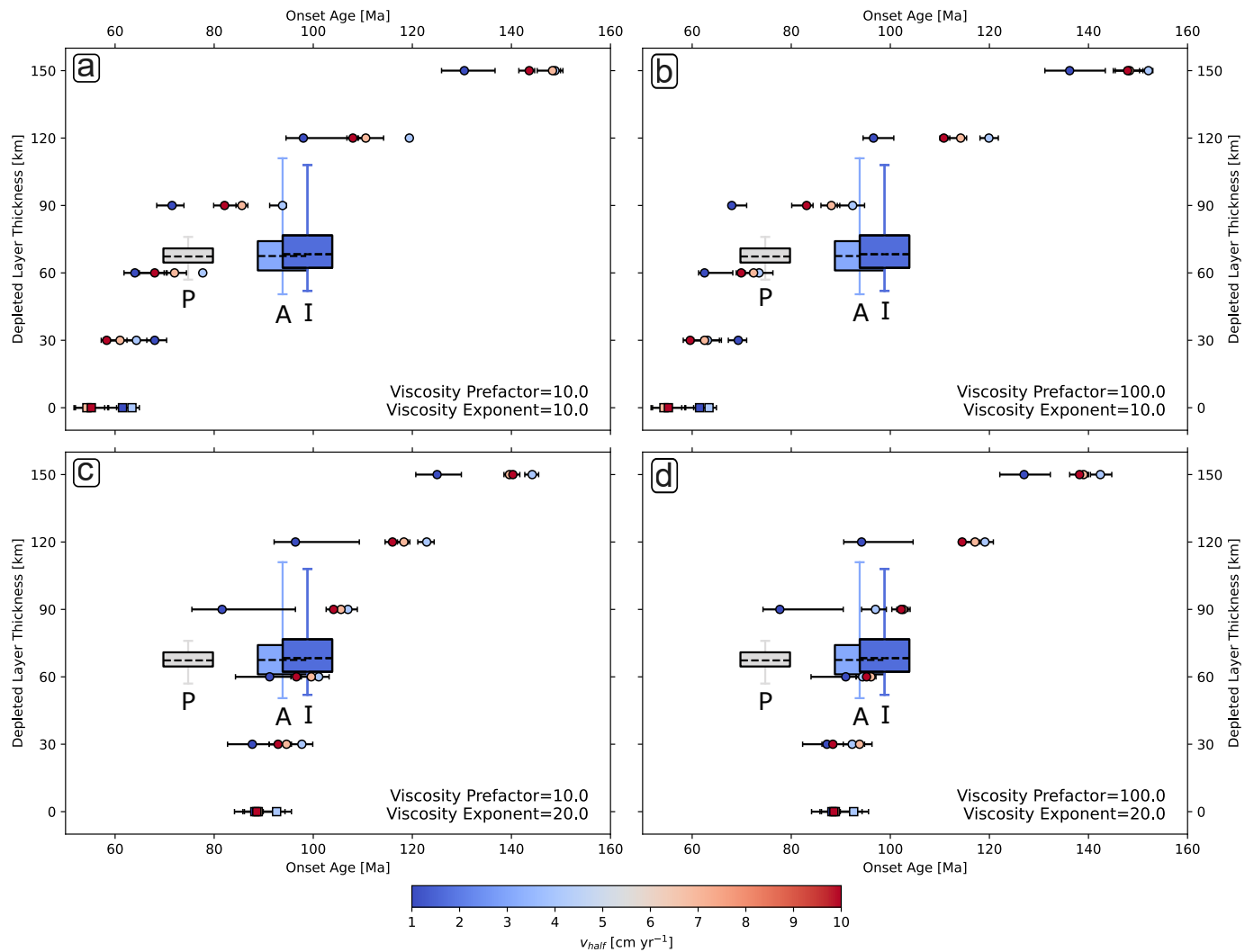


Figure 9. Graphs showing the variability of onset times with varying model parameters of half-spreading rate v_{half} , compositional viscosity prefactor C_η , thermal viscosity exponent α_η , and depleted layer thickness (L_D). Colder colours (blue) to warmer colours (red) represent an increase in plate velocities. (a) Onset times related to models with viscosity Prefactor (C_η) of 10 and viscosity exponent (α_η) of 10 with varying depleted layer thickness and spreading rates. Intervals on boxes and whiskers represent the minimum, lower percentile (16th), median, upper quartile (84th), and maximum values of predicted depleted layer thickness inferred from observed crustal thicknesses (F. D. Richards et al., 2020). Boxes span from lower to upper percentile, with the black line inside the box indicating the median depleted layer thickness of the Pacific (P), Atlantic (A) and Indian (I) basins. Whiskers extend to the minimum and maximum data points of depleted layer thickness. Colour of boxes and whiskers indicate average basin velocities calculated from Seton et al. (2020). The observed onset age range of each basin was calculated using methods outlined in Appendix 2 with the range plotted as ± 5 Ma. Circles = calculated onset age with error bars for each model with colour representing modelled plate velocity; squares = reference models of no depleted layer thickness. (b) Same for models with viscosity Prefactor (C_η) of 100 and viscosity exponent (α_η) of 10. (c) Same for models with viscosity Prefactor (C_η) of 10 and viscosity exponent (α_η) of 20. (d) Same for models with viscosity Prefactor (C_η) of 100 and viscosity exponent (α_η) of 20.

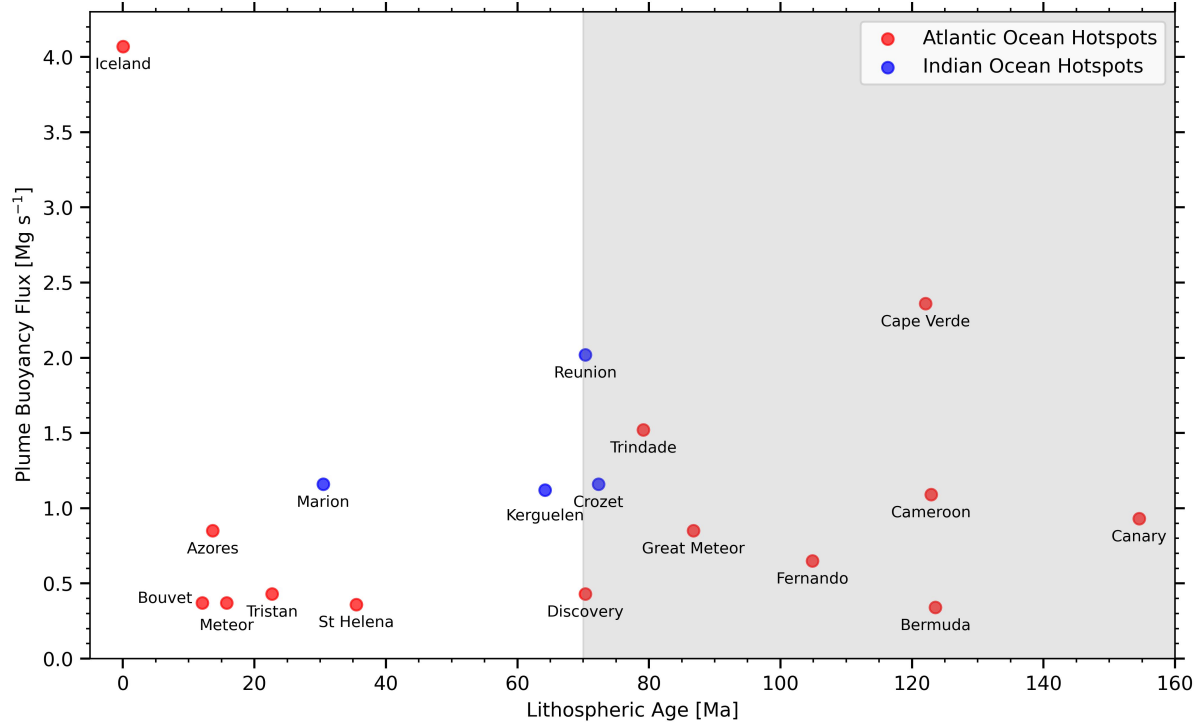


Figure 10. Lithospheric age versus plume buoyancy flux for Atlantic and Indian ocean hotspots. Buoyancy flux data from M. J. Hoggard et al. (2020). Grey box = ages greater than 70 Ma; red circles = Atlantic ocean hotspots; blue circles = Indian ocean hotspots.

of an SCC cell is ~ 100 km (Figure 11), comfortably below the resolution limit of most seismic tomographic models.

Predicted isotherm evolution from SSC models aligns with shear-wave velocity (V_s) observations from seismic tomography (Schaeffer and Lebedev, 2013; F. Richards et al., 2020; Figure 12), suggesting that SSC onset may coincide with flattening and oscillations seen in age-dependent V_s trends at old ages (> 70 Ma). However, the Pacific V_s structure appears to flatten earlier and shallower than predicted by the models (Figure 12a). This discrepancy may result from the models' globally uniform mantle temperature assumption. However, V_s is systematically lower between 150 km and 200 km depth beneath the Pacific Ocean (150 km = $4.31\ km\ s^{-1}$, 200 km = $4.39\ km\ s^{-1}$), compared to the Atlantic and Indian at the same depth (150 km = $4.36\ km\ s^{-1}$, 200 km = $4.43\ km\ s^{-1}$), indicating $\sim 50\text{--}100^\circ\text{C}$ higher mantle temperatures in the Pacific (F. D. Richards et al., 2020). This anomaly amplitude is consistent with the $\sim 50^\circ\text{C}$ higher median temperature found in the deep upper mantle beneath Pacific mid-ocean ridges (Bao et al., 2023).

After comparing model-derived SSC onset times (defined as a 1 km deviation of the 1200°C isotherm from HSC expectations) to onset times that can be visually identified from bathymetry and V_s measurements (Figure 11), it becomes clear that a larger deviation threshold should probably be applied to the model outputs. However, if a higher threshold is chosen, model-derived onset times would become delayed relative to observation-derived counterparts. This potential delay could be reconciled by considering mechanisms that are neglected in my models but are capable of promoting earlier SSC onset. First, dislocation creep may reduce viscosities in the TBL more than envisaged here, especially at high plate velocities, causing

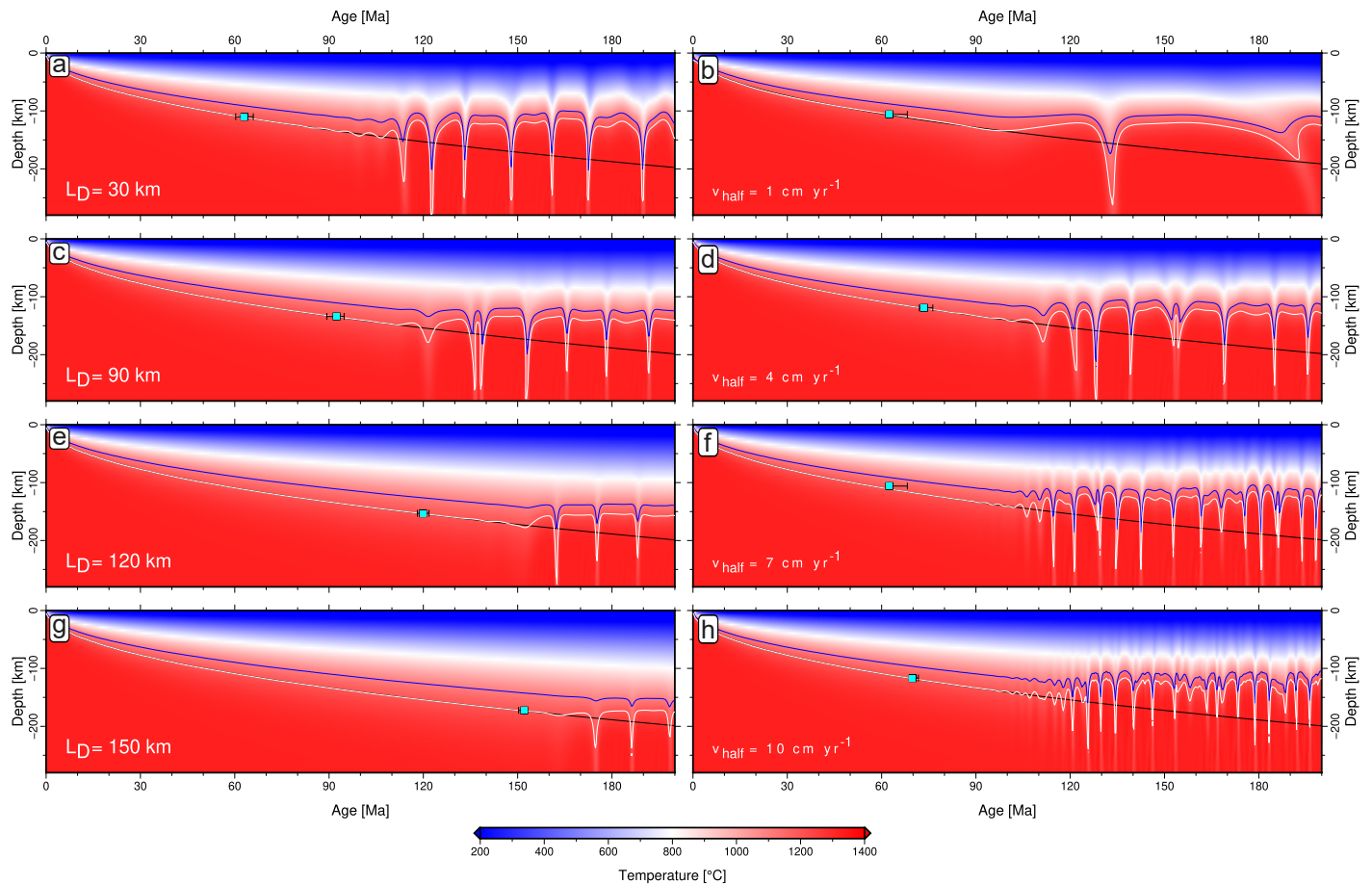


Figure 11. Models of temperature ($^{\circ}\text{C}$) showing the effect of plate speed (v_{half}) and depleted layer thickness (L_D) on SSC onset times. (a) Model with parameters $C_\eta = 100$, $\alpha_\eta = 10$, $v_{\text{half}} = 4 \text{ cm yr}^{-1}$ and $L_D = 30 \text{ km}$. Blue solid line = $1100 \text{ }^{\circ}\text{C}$ isotherm; white solid line = $1200 \text{ }^{\circ}\text{C}$ isotherm; black line = using best fitting isotherm for the model using equation 2; cyan box = shows calculated onset time with error of a standard deviation. (b) Same C_η and α_η but for model $v_{\text{half}} = 1 \text{ cm yr}^{-1}$ and $L_D = 60 \text{ km}$. (c, e & g) Same as (a) but for varying L_D at 90, 120 and 150km respectively. (d, f & h) Same as (b) for varying v_{half} of 4, 7 and 10 cm yr^{-1} , respectively.

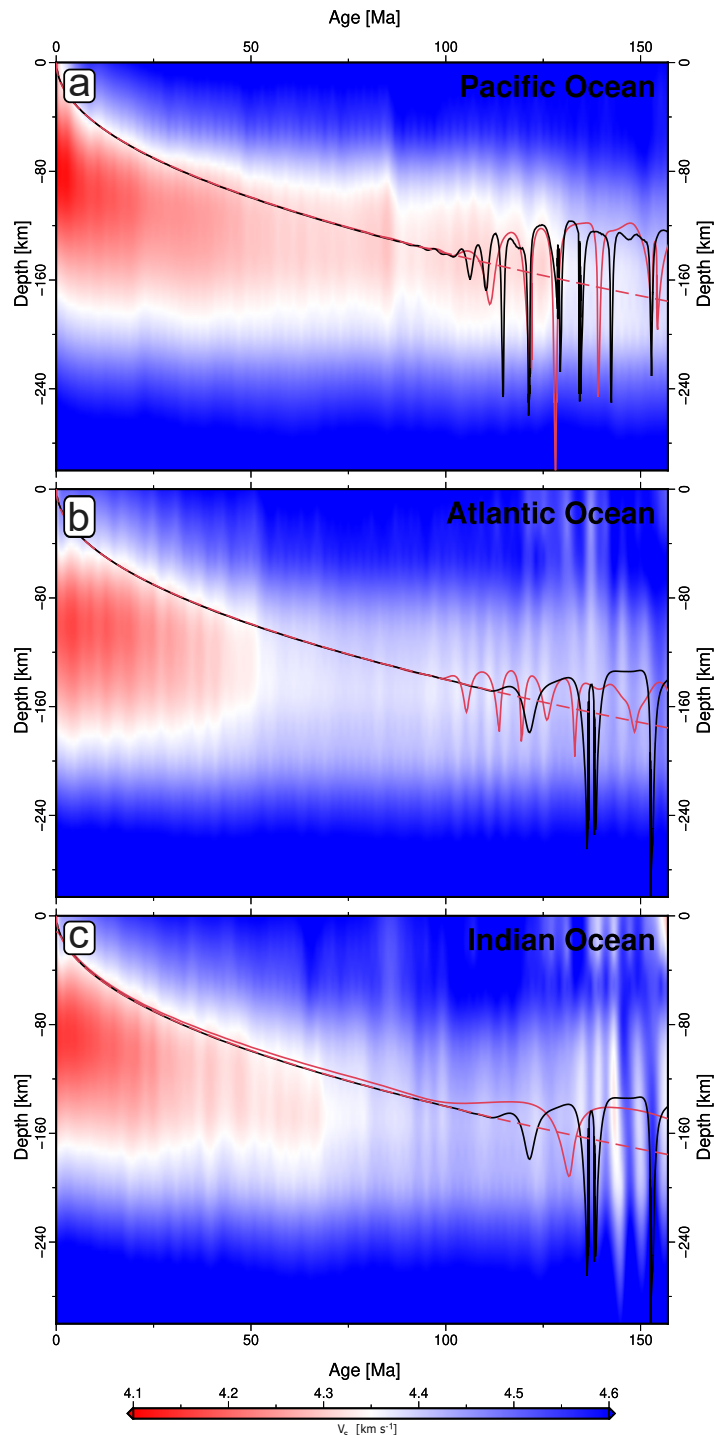


Figure 12. Inter-basin comparison between shear-wave velocities from seismic tomography (Schaeffer and Lebedev, 2013) and predictions from the HSC model and 1200 °C isotherm evolution from "best-fitting" SSC convection models at time-step 300 Ma. Dashed red line = best fitting global HSC calculated from equitation 2. Red solid line = isotherm evolution from "best-fitting" median model for the Pacific subset: $C_\eta = 100$, $\alpha_\eta = 10$, $L_D = 60$ km and $v_{\text{half}} = 4 \text{ cm yr}^{-1}$. Black solid line = upper median "best-fitting" model isotherm evolution for the Pacific subset: $C_\eta = 100$, $\alpha_\eta = 10$, $L_D = 60$ km and $v_{\text{half}} = 7 \text{ cm yr}^{-1}$. (b) same as (a) but for the Atlantic Ocean. Red solid line = model parameters are model $C_\eta = 100$, $\alpha_\eta = 20$, $L_D = 60$ km and $v_{\text{half}} = 4 \text{ cm yr}^{-1}$. Black solid line = model parameters are model $C_\eta = 100$, $\alpha_\eta = 10$, $L_D = 90$ km and $v_{\text{half}} = 4 \text{ cm yr}^{-1}$. (c) same as (a) but for the Indian Ocean. Red solid line = model parameters are model $C_\eta = 100$, $\alpha_\eta = 20$, $L_D = 60$ km and $v_{\text{half}} = 1 \text{ cm yr}^{-1}$. Black solid line = model parameters are model $C_\eta = 100$, $\alpha_\eta = 10$, $L_D = 90$ km and $v_{\text{half}} = 4 \text{ cm yr}^{-1}$. NOTE: even though model parameters with $\alpha_\eta = 20$ were selected as the best fitting models for the Indian and Atlantic regions, $\alpha_\eta = 10$ is generally preferred as those models explain the wide range of onsets we see across the basins (See Figure 9).

the local Rayleigh (Ra) number to exceed the critical value for convective instability earlier (Afonso et al.,

2008). Secondly, adopting values of thermal expansivity that are towards the higher end of experimentally constrained ranges (e.g., $\sim 3\text{--}4 \times 10^{-5} \text{ K}^{-1}$; F. Richards et al., 2018), would accentuate density contrasts across the growing TBL, also reducing the age at which the critical Ra value is surpassed. Finally, the 2D models used in this study can only assess the influence of transverse convective rolls (TR); structures perpendicular to plate motion. However, in 3D models, SSC can develop more complex geometries, including longitudinal rolls (LR or "Richter rolls") that align parallel to the plate motion and may onset more rapidly (Richter and Parsons, 1975; Richter and Parsons, 1975; van Hunen et al., 2003; Huang et al., 2003; Zlotnik et al., 2008). Nevertheless, while these model limitations may lead to some model-data mismatch in absolute SSC onset ages, the model predictions of relative SSC onset time differences as a function of depleted layer thickness and their agreement with observed offsets between ocean basins appear to be robust.

5. Conclusions

This study critically examines various mechanisms that have been proposed to explain observed seafloor flattening, including age-dependent dynamic topography, lithospheric rejuvenation, and small scale convection (SSC). The findings reveal that deep mantle dynamics alone fails to explain the observed flattening signals in all basins. Lithospheric rejuvenation via mantle plumes can explain certain features in the bathymetric trends of each basin, but the overall magnitude and spatial extent of its influence cannot account for global flattening patterns, especially in the Atlantic and Indian Oceans. Nevertheless, despite their relatively limited individual impact, I show that the combined signal of rejuvenation and dynamic topography could explain the enigmatic shoaling of Pacific bathymetry on 80–130 Ma lithosphere.

The dominant mechanism driving seafloor flattening appears to be SSC, with interbasin differences in flattening onset caused by variations in spreading rate and the thickness of melt-depleted layers within the cooling lithosphere. This hypothesis is supported by global correlations between lithospheric and crustal thickness at old ages, indicating that later flattening in the Atlantic and Indian Oceans is linked to higher depleted layer thicknesses within their old lithosphere due to higher axial potential temperatures existing at the time that lithosphere was created. Numerical SSC modelling further confirms this result obtaining differences in onset time as a function of depleted layer thickness that are broadly compatible with crustal-thickness-derived mantle palaeotemperatures and age-dependent shear-wave velocity and basement depth trends in each basin. Overall, my findings suggest that SSC is ubiquitous beneath old oceanic lithosphere, explaining the success of plate cooling models in explaining bathymetric observations. They also imply that interbasin differences in flattening are also SSC-related and caused by mantle-temperature-modulated variations in lithospheric melt depletion, with lithospheric rejuvenation and dynamic topography only able to explain regional deviations from these trends.

Appendix 1. Z16 Fits

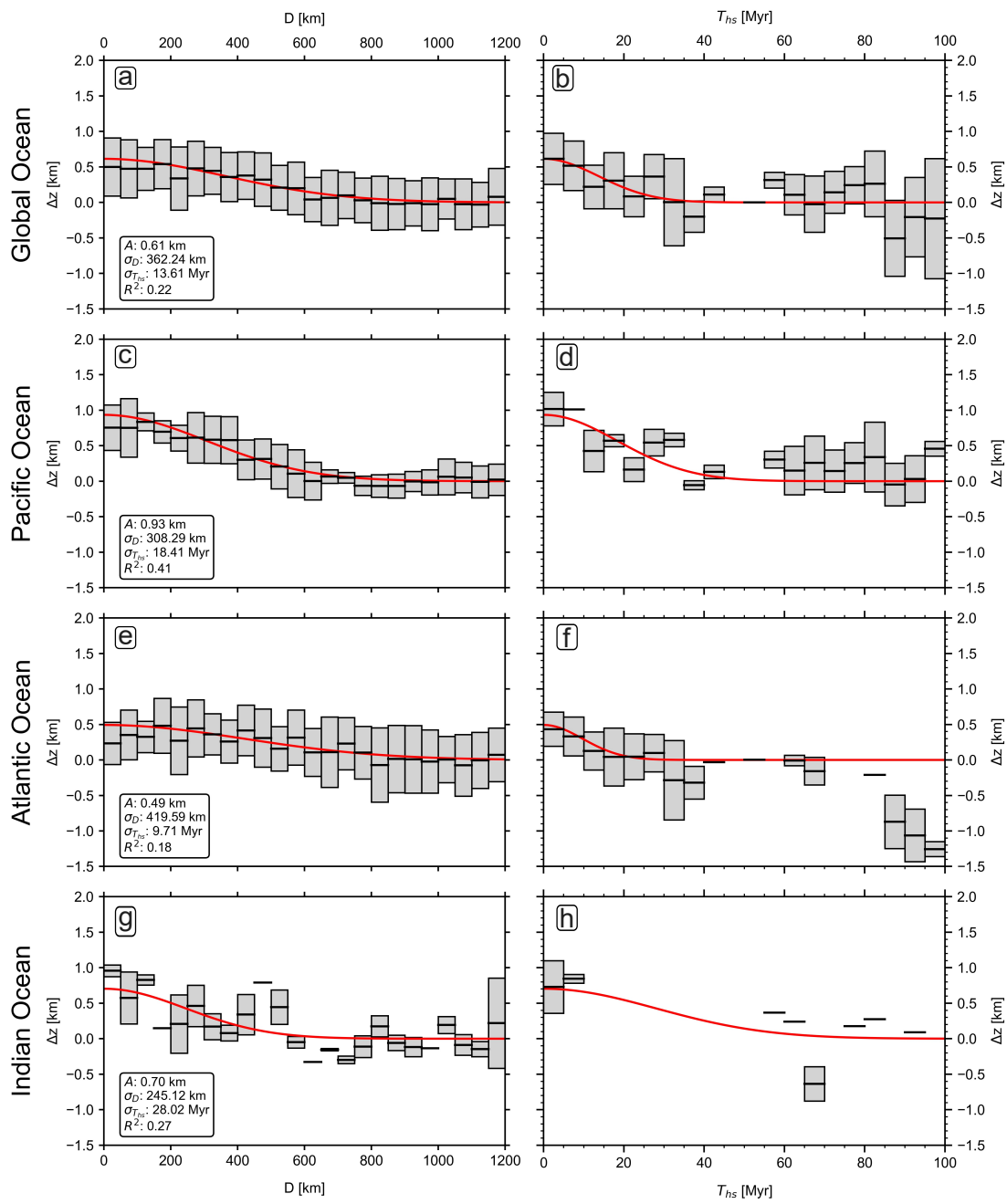


Figure A1. Optimised fits to global and basin-specific residual depth anomaly datasets (Holdt et al., 2022) using the global plate model Zahirovic et al. (2016). (a) Global dataset. Red line = fit of 2D to residual depth anomalies as a function of distance away from hotspot track (D); grey box = standard deviation with the black horizontal line representing the mean, binned at 50-km intervals. The fitted parameters—amplitude in km (A), critical distance in km (σ_D), critical time ($\sigma_{T_{hs}}^2$) and the coefficient of determination (R^2)—are annotated in the bottom left. (b) Same for time elapsed since last hotspot interaction (T_{hs}), binned at 5-Myr intervals. (c, e, & g) Same as (a) for Pacific, Atlantic, and Indian datasets, respectively. (d, f, & h) Same as (b) for Pacific, Atlantic, and Indian datasets, respectively.

Appendix 2. Basin Absolute Onset Calculations

Water-loaded basement depth data (F. Richards et al., 2018) was used for the Pacific, Indian and Pacific basins and fitted to a modified half-space cooling model equation from D. L. Turcotte and Schubert (2002)

for basement depths less than 70 Ma, with data from the anomalously elevated regions around the Iceland hotspot removed. Datapoints from regions of anomalous crust were also excised using the polygons outlined in M. J. Hoggard et al. (2017). HSC predictions of subsidence with age are calculated using the expression

$$w(t) = w_0 + \frac{2\rho_m\alpha\Delta T}{(\rho_m - \rho_w)\sqrt{\pi}}\sqrt{\kappa t}, \quad (\text{A1})$$

where, w is the predicted seafloor in km at age, t (s), w_0 is the zero-age depth in km, ρ_m is mantle density (3300 kg/m^3), ρ_w is water density (1030 kg/m^3), α is thermal expansivity (K^{-1}), κ is thermal diffusivity ($\text{m}^2 \text{ s}^{-1}$), ΔT is the temperature contrast across the lithosphere in K . Free parameters and initial guesses used in the fitting process include:

- w_0 : Initial seafloor depth (km), initial guess = 2, bounds = [1, 4]
- κ : Thermal diffusivity (m^2/s), initial guess = 1×10^{-6} , bounds = [1×10^{-7} , 3×10^{-6}]
- ΔT : Temperature contrast (K), initial guess = 1300, bounds = [1100, 1800]
- α : Thermal expansivity (K^{-1}), initial guess = 2.5×10^{-5} , bounds = [1×10^{-5} , 4×10^{-5}]

Results from fitting equation A1 to the basement depth data in each basin are shown in the table below:

Parameter	Atlantic	Indian	Pacific
w_0 (km)	1.85	2.73	2.61
$\kappa (\times 10^{-6} \text{ m}^2/\text{s})$	1.35	1.29	1.18
ΔT (K)	1386	1373	1347
$\alpha (\times 10^{-5} \text{ K}^{-1})$	2.35	2.29	2.18

Table A1. Estimated parameters after fitting to the HSC model with zero depth (Equation A1) for the Atlantic, Indian, and Pacific basins.

Optimal parameters obtained from the HSC parameter fitting process were then fed into an equivalent PCM using the following expression from D. L. Turcotte and Schubert (2002), adapted to account for the different zero-age depths in each basin,

$$w(t) = w_0 + \frac{\rho_m\alpha\Delta Ty_{L0}}{\rho_m - \rho_w} \left(\frac{1}{2} - \frac{4}{\pi^2} \sum_{m=0}^{10} \frac{\exp\left(-\kappa \frac{(1+2m)^2\pi^2t}{y_{L0}^2}\right)}{(1+2m)^2} \right), \quad (\text{A2})$$

where y_{L0} is lithospheric thickness in km, m is the summation index for the series expansion, and all other parameters are identical to those in Equation A1.

The average lithospheric thickness (y_{L0}) was calculated for each basin, using M. J. Hoggard et al. (2017) polygons remove regions of anomalous crust. Then using calibrated conversions of the global seismic tomographic model (SL2013sv; Schaeffer and Lebedev, 2013) average lithospheric thickness of each basin was found (refer to Section 4.1.1 for a description). y_{L0} was then applied in the PCM equation (Equation A2) for each basin alongside best-fit results from Equation A1. Estimated y_{L0} was 105 km, 118 km, and 119 km for the Pacific, Indian and Atlantic basins, respectively.

SSC onset times for each basin were then calculated as based on the age at which HSC- and PCM-predicted basement depths diverged by more than the uncertainty in the each basement depth dataset (M. J. Hoggard et al., 2017). The critical uncertainty values were calculated by binning the data into 5

Ma intervals. For each bin, the mean and standard deviation were computed, and the uncertainties were combined across all bins to determine the overall dataset uncertainty. The critical uncertainties used were 0.36 km, 0.55 km, and 0.56 km for the Pacific, Atlantic, and Indian basins, respectively, resulting in SSC onset times of 75 Ma, 94 Ma, and 99 Ma. (Figure A2)

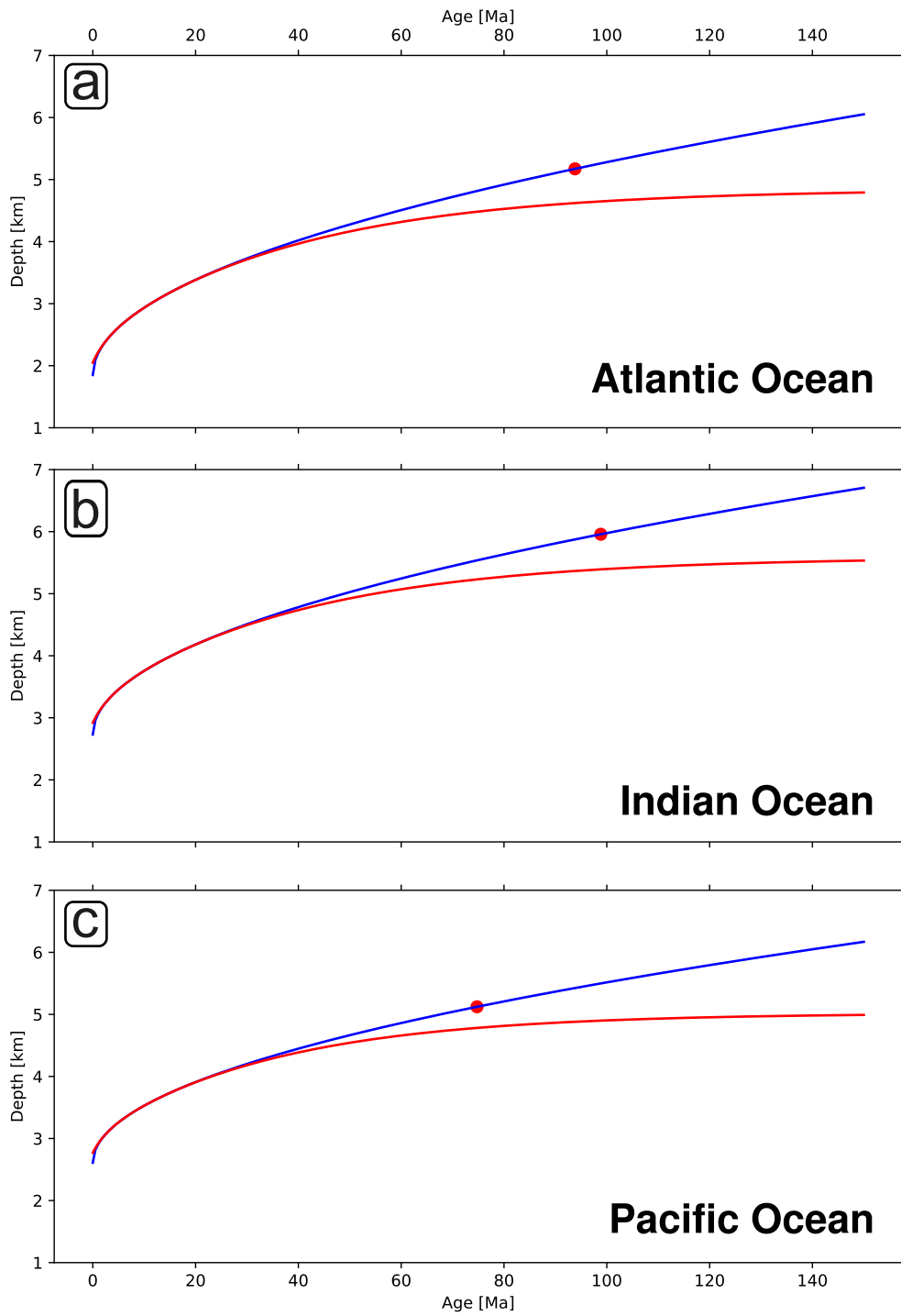


Figure A2. Interbasin comparison of calculated onset time. Results from fitting HSC and PCM parameterisations (Equations A1 and A2). (a) Blue line = calculated HSC model from Atlantic water-loaded basement depth data of F. Richards et al. (2018); red line = calculated PCM model from water-loaded basement depth data from F. Richards et al. (2018); red dot = inferred onset time. (b) Same for the Indian data subset. (c) Same for the Pacific data subset.

■ Acknowledgements

Firstly, I would like to thank Dr. Fred Richards for his continued support throughout this project. His guidance, expertise, and encouragement have been invaluable in helping me navigate all the challenges I faced during this project and to ultimately achieve all goals outlined. Thank you for your mentorship and belief in my abilities.

Secondly, a massive thank you goes to Anita Murphy for being supportive and always providing time for me. She has been a cornerstone throughout my time at university.

I also thank the Computational Infrastructure for Geodynamics (geodynamics.org) which is funded by the National Science Foundation under award EAR-0949446 and EAR-1550901 for supporting the development of ASPECT. Furthermore

Overleaf template by Authors: Guillermo Jimenez (memo.notess1@gmail.com) and Eduardo Gracidas (eduardo.gracidas29@gmail.com) - Rho LaTeX Template Version 2.0.0 (21/05/2024).

To ensure transparency and uphold academic integrity, the following outlines AI use in this report. Generative AI (ChatGPT) was used in the aid of plotting and analysing data for some plots made using Python scripts. Grammarly was used to highlight grammar, spelling and punctuation inconsistencies in text. Furthermore, it highlighted redundant words/phrases, sometimes providing alternative solutions. Wordfull (AI in Overleaf) was used to help make tables.

■ References

- Afonso, J. C., Zlotnik, S., & Fernandez, M. (2008). Effects of compositional and rheological stratifications on small-scale convection under the oceans: Implications for the thickness of oceanic lithosphere and seafloor flattening. *Geophysical Research Letters*, 35(20). <https://doi.org/10.1029/2008GL035419>
- Agrusta, R., Arcay, D., Tommasi, A., Davaille, A., Ribe, N., & Gerya, T. (2013). Small-scale convection in a plume-fed low-viscosity layer beneath a moving plate. *Geophysical Journal International*, 194(2), 591–610. <https://doi.org/10.1093/gji/ggt128>
- Agrusta, R., Tommasi, A., Arcay, D., Gonzalez, A., & Gerya, T. (2015). How partial melting affects small-scale convection in a plume-fed sublithospheric layer beneath fast-moving plates. *Geochemistry, Geophysics, Geosystems*, 16(11), 3924–3945. <https://doi.org/10.1002/2015GC005967>
- Ball, P., White, N., MacLennan, J., & Stephenson, S. (2021). Global influence of mantle temperature and plate thickness on intraplate volcanism. *Nature Communications*, 12(1), 2045. <https://doi.org/10.1038/s41467-021-22323-9>
- Ballmer, M., Van Hunen, J., Ito, G., Tackley, P., & Bianco, T. (2007). Non-hotspot volcano chains originating from small-scale sublithospheric convection. *Geophysical Research Letters*, 34(23). <https://doi.org/10.1029/2007GL031636>
- Bangerth, W., Dannberg, J., Fraters, M., Gassmoeller, R., Glerum, A., Heister, T., Myhill, R., & Naliboff, J. (2023, July). *Aspect v2.5.0* (Version v2.5.0). Zenodo. <https://doi.org/10.5281/zenodo.8200213>
- Bao, X., Mittal, T., & Lithgow-Bertelloni, C. (2023). Determining mid-ocean ridge geography from upper mantle temperature. *Authorea Preprints*. d197for5662m48.cloudfront.net/documents/publicationstatus/130555/preprint.pdf/47292364b78818df30783e6e161b0439.pdf
- Buck, W. R., & Parmentier, E. (1986). Convection beneath young oceanic lithosphere: Implications for thermal structure and gravity. *Journal of Geophysical Research: Solid Earth*, 91(B2), 1961–1974. <https://doi.org/10.1029/JB091iB02p01961>
- Christeson, G., Goff, J., & Reece, R. (2019). Synthesis of oceanic crustal structure from two-dimensional seismic profiles. *Reviews of Geophysics*, 57(2), 504–529. <https://doi.org/10.1029/2019RG000641>
- Coltice, N., & Shephard, G. E. (2018). Tectonic predictions with mantle convection models. *Geophysical Journal International*, 213(1), 16–29. <https://doi.org/10.1093/gji/ggx531>
- Conrad, C. P., & Lithgow-Bertelloni, C. (2006). Influence of continental roots and asthenosphere on plate-mantle coupling. *Geophysical Research Letters*, 33(5). <https://doi.org/10.1029/2005GL025621>
- Crosby, A., & McKenzie, D. (2009). An analysis of young ocean depth, gravity and global residual topography. *Geophysical Journal International*, 178(3), 1198–1219. <https://doi.org/10.1029/JB082i005p00803>
- Crosby, A., McKenzie, D., & Slater, J. (2006). The relationship between depth, age and gravity in the oceans. *Geophysical Journal International*, 166(2), 553–573. <https://doi.org/10.1111/j.1365-246X.2006.03015.x>
- Crough, S. T. (1978). Thermal origin of mid-plate hot-spot swells. *Geophysical Journal International*, 55(2), 451–469. <https://doi.org/10.1111/j.1365-246X.1978.tb04282.x>
- Davaille, A., & Jaupart, C. (1994). Onset of thermal convection in fluids with temperature-dependent viscosity: Application to the oceanic mantle. *Journal of Geophysical Research: Solid Earth*, 99(B10), 19853–19866. <https://doi.org/10.1029/94JB01405>

- Davies. (2011). *Mantle convection for geologists*. Cambridge University Press.
- de Carvalho, J. F. S. (2020). *Imaging the cape verde hotspot structure* [Doctoral dissertation, Universidade de Lisboa (Portugal)]. www.proquest.com/openview/a39d6b444f572f9457a71c9cdb829d69/1?pq-origsite=gscholar&cbl=2026366&diss=y
- Debayle, E., Dubuffet, F., & Durand, S. (2016). An automatically updated s-wave model of the upper mantle and the depth extent of azimuthal anisotropy. *Geophysical Research Letters*, 43(2), 674–682. <https://doi.org/10.1002/2015GL067329>
- Eilon, Z. C., Zhang, L., Gaherty, J. B., Forsyth, D. W., & Russell, J. B. (2022). Sub-lithospheric small-scale convection tomographically imaged beneath the pacific plate. *Geophysical Research Letters*, 49(18), e2022GL100351. <https://doi.org/10.1029/2022GL100351>
- Flament, N., Gurnis, M., & Müller, R. D. (2013). A review of observations and models of dynamic topography. *Lithosphere*, 5(2), 189–210. <https://doi.org/10.1130/L245.1>
- Heestand, R. L., & Crough, S. T. (1981). The effect of hot spots on the oceanic age-depth relation. *Journal of Geophysical Research: Solid Earth*, 86(B7), 6107–6114. <https://doi.org/10.1029/JB086iB07p06107>
- Heister, T., Dannberg, J., Gassmöller, R., & Bangerth, W. (2017). High accuracy mantle convection simulation through modern numerical methods. II: Realistic models and problems. *Geophysical Journal International*, 210(2), 833–851. <https://doi.org/10.1093/gji/ggx195>
- Herath, P., Stern, T. A., Savage, M. K., Bassett, D., Henrys, S., & Boulton, C. (2020). Hydration of the crust and upper mantle of the hikurangi plateau as it subducts at the southern hikurangi margin. *Earth and Planetary Science Letters*, 541, 116271. <https://doi.org/10.1016/j.epsl.2020.116271>
- Ho, T., Priestley, K., & Debayle, E. (2016). A global horizontal shear velocity model of the upper mantle from multimode love wave measurements. *Geophysical journal international*, 207(1), 542–561. <https://doi.org/10.1093/gji/ggw292>
- Hoggard, K., Richards, F. D., Huston, D. L., Jaques, A. L., & Ghelichkhan, S. (2020). Global distribution of sediment-hosted metals controlled by craton edge stability. *Nature Geoscience*, 13(7), 504–510. <https://doi.org/10.1038/s41561-020-0593-2>
- Hoggard, M. J., Parnell-Turner, R., & White, N. (2020). Hotspots and mantle plumes revisited: Towards reconciling the mantle heat transfer discrepancy. *Earth and Planetary Science Letters*, 542, 116317. <https://doi.org/10.1016/j.epsl.2020.116317>
- Hoggard, M. J., Winterbourne, J., Czarnota, K., & White, N. (2017). Oceanic residual depth measurements, the plate cooling model, and global dynamic topography. *Journal of Geophysical Research: Solid Earth*, 122(3), 2328–2372.
- Holdt, M., White, N., Stephenson, S., & Conway-Jones, B. (2022). Densely sampled global dynamic topographic observations and their significance. *Journal of Geophysical Research: Solid Earth*, 127(7), e2022JB024391. <https://doi.org/10.1029/2022JB024391>
- Huang, J., & Zhong, S. (2005). Sublithospheric small-scale convection and its implications for the residual topography at old ocean basins and the plate model. *Journal of Geophysical Research: Solid Earth*, 110(B5). <https://doi.org/10.1029/2004JB003153>
- Huang, J., Zhong, S., & van Hunen, J. (2003). Controls on sublithospheric small-scale convection. *Journal of Geophysical Research: Solid Earth*, 108(B8). <https://doi.org/10.1029/2003JB002456>

- Humlera, E., Langmuir, C., & Dauxe, V. (1999). Depth versus age: New perspectives from the chemical compositions of ancient crust. *Earth and Planetary Science Letters*, 173(1-2), 7–23. [https://doi.org/10.1016/S0012-821X\(99\)00218-6](https://doi.org/10.1016/S0012-821X(99)00218-6)
- Huppert, K. L., Perron, J. T., & Royden, L. H. (2020). Hotspot swells and the lifespan of volcanic ocean islands. *Science advances*, 6(1), eaaw6906. <https://doi.org/10.1126/sciadv.aaw6906>
- Korenaga, J. (2003). Energetics of mantle convection and the fate of fossil heat. *Geophysical Research Letters*, 30(8). <https://doi.org/10.1029/2003gl016982>
- Korenaga, J. (2008). Urey ratio and the structure and evolution of earth's mantle. *Reviews of Geophysics*, 46(2). <https://doi.org/10.1029/2007RG000241>
- Korenaga, J. (2015). Seafloor topography and the thermal budget of earth. *Geol. Soc. Am. Spec. Pap.*, 514, 167–185.
- Korenaga, J. (2020). Plate tectonics and surface environment: Role of the oceanic upper mantle. *Earth-science reviews*, 205, 103185. <https://doi.org/10.1016/j.earscirev.2020.103185>
- Korenaga, T., & Korenaga, J. (2016). Evolution of young oceanic lithosphere and the meaning of seafloor subsidence rate. *Journal of Geophysical Research: Solid Earth*, 121(9), 6315–6332. <https://doi.org/10.1002/2016JB013395>
- Korenaga, T., Korenaga, J., Kawakatsu, H., & Yamano, M. (2021). A new reference model for the evolution of oceanic lithosphere in a cooling earth. *Journal of Geophysical Research: Solid Earth*, 126(6), e2020JB021528. <https://doi.org/10.1029/2020JB021528>
- Kronbichler, M., Heister, T., & Bangerth, W. (2012). High accuracy mantle convection simulation through modern numerical methods. *Geophysical Journal International*, 191, 12–29. <https://doi.org/10.1111/j.1365-246X.2012.05609.x>
- Lee, C.-T. A., Lenardic, A., Cooper, C. M., Niu, F., & Levander, A. (2005). The role of chemical boundary layers in regulating the thickness of continental and oceanic thermal boundary layers. *Earth and Planetary Science Letters*, 230(3-4), 379–395. <https://doi.org/10.1016/j.epsl.2004.11.019>
- Li, X., Kind, R., Yuan, X., Wölbern, I., & Hanka, W. (2004). Rejuvenation of the lithosphere by the hawaiian plume. *Nature*, 427(6977), 827–829. <https://doi.org/10.1038/nature02349>
- Ma, Z., & Dalton, C. A. (2019). Evidence for dehydration-modulated small-scale convection in the oceanic upper mantle from seafloor bathymetry and rayleigh wave phase velocity. *Earth and Planetary Science Letters*, 510, 12–25. <https://doi.org/10.1016/j.epsl.2018.12.030>
- McKenzie, D., Jackson, J., & Priestley, K. (2005). Thermal structure of oceanic and continental lithosphere. *Earth and Planetary Science Letters*, 233(3-4), 337–349. <https://doi.org/10.1016/j.epsl.2005.02.005>
- McKenzie, D., & Weiss, N. (1975). Speculations on the thermal and tectonic history of the earth. *Geophysical Journal International*, 42(1), 131–174. <https://doi.org/10.1111/j.1365-246X.1975.tb05855.x>
- Monnereau, M., Rabinowicz, M., & Arquis, E. (1993). Mechanical erosion and reheating of the lithosphere: A numerical model for hotspot swells. *Journal of Geophysical Research: Solid Earth*, 98(B1), 809–823. <https://doi.org/10.1029/92JB01677>
- Müller, R. D., Cannon, J., Qin, X., Watson, R. J., Gurnis, M., Williams, S., Pfaffelmoser, T., Seton, M., Russell, S. H., & Zahirovic, S. (2018). Gplates: Building a virtual earth through deep time. *Geochemistry, Geophysics, Geosystems*, 19(7), 2243–2261. <https://doi.org/10.1029/2018GC007584>

- Müller, R. D., Flament, N., Cannon, J., Tetley, M. G., Williams, S. E., Cao, X., Bodur, Ö. F., Zahirovic, S., & Merdith, A. (2022). A tectonic-rules-based mantle reference frame since 1 billion years ago—implications for supercontinent cycles and plate–mantle system evolution. *Solid Earth*, 13(7), 1127–1159. <https://doi.org/10.5194/se-13-1127-2022>
- Müller, R. D., Sdrolias, M., Gaina, C., & Roest, W. R. (2008). Age, spreading rates, and spreading asymmetry of the world's ocean crust. *Geochemistry, Geophysics, Geosystems*, 9(4). <https://doi.org/10.1029/2007GC001743>
- Müller, R. D., Seton, M., Zahirovic, S., Williams, S. E., Matthews, K. J., Wright, N. M., Shephard, G. E., Maloney, K. T., Barnett-Moore, N., Hosseinpour, M., et al. (2016). Ocean basin evolution and global-scale plate reorganization events since pangea breakup. *Annual Review of Earth and Planetary Sciences*, 44(1), 107–138. <https://doi.org/10.1146/annurev-earth-060115-012211>
- Parker, R., & Oldenburg, D. (1973). Thermal model of ocean ridges. *Nature Physical Science*, 242(122), 137–139. <https://doi.org/10.1038/physci242137a0>
- Parsons, B., & McKenzie, D. (1978). Mantle convection and the thermal structure of the plates. *Journal of Geophysical Research: Solid Earth*, 83(B9), 4485–4496. <https://doi.org/10.1029/JB083iB09p04485>
- Parsons, B., & Sclater, J. G. (1977). An analysis of the variation of ocean floor bathymetry and heat flow with age. *Journal of geophysical research*, 82(5), 803–827. <https://doi.org/10.1029/JB082i005p00803>
- Ribe, N. M. (2004). Through thick and thin. *Nature*, 427(6977), 793–795. <https://doi.org/10.1038/427793a>
- Richards, F., Hoggard, M., Cowton, L., & White, N. (2018). Reassessing the thermal structure of oceanic lithosphere with revised global inventories of basement depths and heat flow measurements. *Journal of Geophysical Research: Solid Earth*, 123(10), 9136–9161. <https://doi.org/10.1029/2018JB015998>
- Richards, F., Hoggard, M., Crosby, A., Ghelichkhan, S., & White, N. (2020). Structure and dynamics of the oceanic lithosphere–asthenosphere system. *Physics of the Earth and Planetary Interiors*, 309, 106559. <https://doi.org/10.1016/j.pepi.2020.106559>
- Richards, F. D., Hoggard, M. J., Ghelichkhan, S., Koelemeijer, P., & Lau, H. C. (2023). Geodynamic, geodetic, and seismic constraints favour deflated and dense-cored Ilvps. *Earth and Planetary Science Letters*, 602, 117964. <https://doi.org/10.1016/j.epsl.2022.117964>
- Richards, F. D., Hoggard, M. J., White, N., & Ghelichkhan, S. (2020). Quantifying the relationship between short-wavelength dynamic topography and thermomechanical structure of the upper mantle using calibrated parameterization of anelasticity. *Journal of Geophysical Research: Solid Earth*, 125(9), e2019JB019062. <https://doi.org/10.1029/2019JB019062>
- Richter, F. M. (1973). Convection and the large-scale circulation of the mantle. *Journal of Geophysical Research*, 78(35), 8735–8745. <https://doi.org/10.1029/JB078i035p08735>
- Richter, F. M., & Parsons, B. (1975). On the interaction of two scales of convection in the mantle. *Journal of Geophysical Research*, 80(17), 2529–2541. <https://doi.org/10.1029/JB080i017p02529>
- Schaeffer, A., & Lebedev, S. (2013). Global shear speed structure of the upper mantle and transition zone. *Geophysical Journal International*, 194(1), 417–449. <https://doi.org/10.1093/gji/ggt095>
- Seton, M., Müller, R. D., Zahirovic, S., Williams, S., Wright, N. M., Cannon, J., Whittaker, J. M., Matthews, K. J., & McGirr, R. (2020). A global data set of present-day oceanic crustal age and seafloor

- spreading parameters. *Geochemistry, Geophysics, Geosystems*, 21(10), e2020GC009214. <https://doi.org/10.1029/2020GC009214>
- Shorttle, O., MacLennan, J., & Lambart, S. (2014). Quantifying lithological variability in the mantle. *Earth and Planetary Science Letters*, 395, 24–40. <https://doi.org/10.1016/j.epsl.2014.03.040>
- Sleep, N. H. (2011). Small-scale convection beneath oceans and continents. *Chinese Science Bulletin*, 56, 1292–1317. <https://doi.org/10.1007/s11434-011-4435-x>
- Stein, C. A., & Stein, S. (1992). A model for the global variation in oceanic depth and heat flow with lithospheric age. *Nature*, 359(6391), 123–129.
- Steinberger, B., & Torsvik, T. H. (2008). Absolute plate motions and true polar wander in the absence of hotspot tracks. *Nature*, 452(7187), 620–623. <https://doi.org/10.1038/nature06824>
- Tetley, M. G., Williams, S. E., Gurnis, M., Flament, N., & Müller, R. D. (2019). Constraining absolute plate motions since the triassic. *Journal of Geophysical Research: Solid Earth*, 124(7), 7231–7258. <https://doi.org/10.1029/2019JB017442>
- Thoraval, C., Tommasi, A., & Doin, M.-P. (2006). Plume-lithosphere interaction beneath a fast moving plate. *Geophysical research letters*, 33(1). <https://doi.org/10.1029/2005GL024047>
- Torsvik, T. H., Müller, R. D., Van der Voo, R., Steinberger, B., & Gaina, C. (2008). Global plate motion frames: Toward a unified model. *Reviews of geophysics*, 46(3). <https://doi.org/10.1029/2007RG000227>
- Turcotte, D., & Oxburgh, E. (1967). Finite amplitude convective cells and continental drift. *Journal of Fluid Mechanics*, 28(1), 29–42. <https://doi.org/10.1017/S0022112067001880>
- Turcotte, D. L., & Schubert, G. (2002). *Geodynamics*. Cambridge university press.
- Utada, H. (2019). Ocean bottom geophysical array studies may reveal the cause of seafloor flattening. *Earth and Planetary Science Letters*, 518, 100–107. <https://doi.org/10.1016/j.epsl.2019.04.040>
- van Hunen, J., Huang, J., & Zhong, S. (2003). The effect of shearing on the onset and vigor of small-scale convection in a newtonian rheology. *Geophysical research letters*, 30(19). <https://doi.org/10.1029/2003GL018101>
- Vidal, V., & Bonneville, A. (2004). Variations of the hawaiian hot spot activity revealed by variations in the magma production rate. *Journal of Geophysical Research: Solid Earth*, 109(B3). <https://doi.org/10.1029/2003JB002559>
- Wessel, P. (1999). New hotspotting tools released. *in Proceedings, EOS Trans, AGU*, 80(29), 319.
- Winterbourne, J., Crosby, A., & White, N. (2009). Depth, age and dynamic topography of oceanic lithosphere beneath heavily sedimented atlantic margins. *Earth and Planetary Science Letters*, 287(1-2), 137–151. <https://doi.org/10.1016/j.epsl.2009.08.019>
- Young, A., Flament, N., Maloney, K., Williams, S., Matthews, K., Zahirovic, S., & Müller, R. D. (2019). Global kinematics of tectonic plates and subduction zones since the late paleozoic era. *Geoscience Frontiers*, 10(3), 989–1013. <https://doi.org/10.1016/j.gsf.2018.05.011>
- Zahirovic, S., Matthews, K. J., Flament, N., Müller, R. D., Hill, K. C., Seton, M., & Gurnis, M. (2016). Tectonic evolution and deep mantle structure of the eastern tethys since the latest jurassic. *Earth-Science Reviews*, 162, 293–337. <https://doi.org/10.1016/j.earscirev.2016.09.005>

- Zaranek, S. E., & Parmentier, E. (2004). The onset of convection in fluids with strongly temperature-dependent viscosity cooled from above with implications for planetary lithospheres. *Earth and Planetary Science Letters*, 224(3-4), 371–386. <https://doi.org/10.1016/j.epsl.2004.05.013>
- Zlotnik, S., Afonso, J. C., Díez, P., & Fernández, M. (2008). Small-scale gravitational instabilities under the oceans: Implications for the evolution of oceanic lithosphere and its expression in geophysical observables. *Philosophical Magazine*, 88(28-29), 3197–3217. <https://doi.org/10.1080/14786430802464248>